The combined inversion of seismological and GOCE gravity data: New insights into the current state of the Pacific lithosphere and upper mantle

Rosaria Tondi[1], Maddalena Gilardoni[2], Mirko Reguzzoni[2]

[1]*Istituto Nazionale di Geofisica e Vulcanologia, Via Donato Creti 12, 40128 Bologna, sezione di Bologna, Italy*

[2]*DICA, Politecnico di Milano, P.zza Leonardo da Vinci 32, 20133 Milano, Italy*

Formatted: Italian (Italy)

ABSTRACT

~~We~~In this study we combine seismological and GOCE satellite gravity information ~~with~~by using a Bayesian-like technique, ~~for~~with the aim of inferring the density structure of the Pacific~~-~~ (90°N 90°S) (121°E 60°W) lithosphere and upper mantle.

We recover a 1° x 1° 3-D density model, down to ~~a~~ 300 km depth, which explains gravity observations with a variance reduction of 67.41%. ~~-~~The model, with an associated *a posteriori* standard deviation ~~ranging between 2.6 and 75.4 kg/m^3~~, provides a significant contribution to understanding the ~~dynamic processes of the oceanic lithosphere~~ evolution of the Pacific ~~plate~~lithosphere and answer to some debated geodynamic questions.

~~Additionally, we exploit the possibility of recovering a 3D map of the density-v$_S$ couplings throughout the whole structure, in order to identify the regions characterized by chemically-induced density anomalies and to distinguish them from the thermally induced anomalies. This information, together with a qualitative analysis of the interplay between the surface topography and the mantle flows, enables us to make inferences regarding the dynamic surface~~

~~topography and the composition of the Pacific lithosphere. We conjecture that the chemically modified composition of the oceanic lithosphere may reconcile both seismological, geodetic and heat flow observations both below the northwestern side of the Pacific Plate and in the region beneath the Pacific Superswell.~~

Our methodology enables us to combine the recovery of density parameters with the optimum density-v_{SV} scalings. The latter account for both seismological and gravity observations in order to identify the regions characterized by chemically-induced density heterogeneities which add to the thermally-induced anomalies. Chemically-modified structures are found west of the East Pacific Rise (EPR) and are of relevant amplitude both below the north-western side of the Pacific Plate, at the base of the lithosphere, and up to 100 km depth beneath the Hawaiian and Super Swell regions, thus explaining the anomalous shallow regions without invoking as the sole justification the thermal buoyancy. Coherently with the chemically modified structures, our results a) support a lighter and more buoyant lithosphere than that predicted by the cooling models and b) are in favor of the hypothesized crustal underplating beneath the Hawaiian chain and beneath the volcanic units in the southern branch of the Super Swell region. The comparison between calculated mantle gravity residuals and residual topography suggests a) a lateral viscosity growth associated with the increasing thickness and density of the Plate and b) correlate well with sub-lithospheric mantle flow from the EPR towards west, up to the Kermadec and Tonga Trench in the south and the Kuril-Kamchatka Trench in the north.

1. INTRODUCTION

The topography of the Earth's surface is explained by the combined effects of shallow processes such as erosion or sedimentation, and deeper ones such as isostatic compensation and the upward push/downward pull associated with a convective flow in the mantle (Richards and Hager, 1984). The latter effect, known as dynamic topography, has been evaluated in a number of studies, where models of mantle density are defined on the basis of seismic tomography, and used to predict the associated mantle flow (Forte, 2007, Boschi et al., 2010, Dávila and Lithgow-Bertelloni, 2013, Flament et al., 2013). Yet, given the number of dynamic processes that affect the topography, researchers still haven't reached a consensus about the term "dynamic topography" and the absence of a detailed knowledge of the thermal and chemical structure of the lithosphere, effectively limits the possibility to discriminate among a number of different solutions. As an example, the bathymetry of the young ocean floor (<80 Ma) is compatible with that of the thermal boundary layer of the convecting mantle, and, in this respect, the subsidence of oceanic lithosphere with age should be included in the definition of dynamic topography. On the other side, ocean floor older than ca. 80 Ma appears to flatten compared to the two main boundary-layer cooling models (McKenzie, 1967, Stein and Stein, 1992, Parker and Oldenburg, 1973), which have been produced to explain the observed variation of heat flow and oceanic depth with age. Additionally, due to its long and complex tectonic history, the dynamics of the continental lithosphere cannot be explained by a boundary layer theory.

~~Unfortunately, given the number of dynamic processes that affect the topography, to date geophysicists have still not found direct evidence from surface observables of convection in the Earth's mantle. Seismically derived models of dynamic topography~~Goal of this paper is to obtain means for constraining

Formatted: Indent: First line: 1.25 cm, Don't add space between paragraphs of the same style

convective circulation of the sub-lithospheric mantle of the Pacific Plate through the analysis of the physical parameters of the oceanic lithosphere. The Pacific region is a natural laboratory for oceanic plate tectonics and it contains not only relatively large areas of old seafloor, but also numerous hot spot tracks, that may have a role in transporting heat to the bottom of the thermal boundary layer. As recalled above, numerous studies have found that seafloor older than 80 Ma reaches depths several hundred meters shallower than would be predicted by the two main lithospheric cooling models (McKenzie, 1967, Stein and Stein, 1992, Parker and Oldenburg, 1973) and no general consensus has yet emerged on a single mechanism of heating that can explain all available observations. Several recent studies have continued to refine these early interpretations of a seafloor depth-age relationship. Proposed explanations include constant heat flux from below (Doin and Fleitout, 1996), thermal rejuvenation by hotspots (Smith and Sandwell, 1997), small-scale convection (e.g., Afonso et al., 2008), dynamic support by mantle flow (Kido and Seno, 1994; Zhang et al., 2012), and departure from the topography predicted by thermal boundary layer theory due to radioactive heat production within the mantle (Jarvis and Peltier, 1982).

In any case, the sophistication and complexity of numerical approaches to determine the role of mantle-lithosphere interactions in shaping surface topography, cannot exempt researchers from studying and reconstructing the fine-scale structure of the lithosphere.

Seismically derived models of lithosphere suffer from incomplete ray coverage or limited data resolution, especially above oceans, where seismic stations, almost exclusively land based, are concentrated at the borders of the seafloor. For example, on the basis of the surface wave tomography of the Pacific mantle,

Ritzwoller et al. (2004) have suggested that old lithosphere does not follow half-space cooling, however the spatial resolution of their tomography does not enable them to rule out that there may be a flattening effect of hotspot chains and oceanic plateaus.

On the other hand, surface observables such as gravity fields and geoid, which are directly dependent on the structure of the underlying distribution of mass, and recently benefit from the information released by space gravity missions such as GRACE and GOCE, are far superior in terms of spatial resolution, but still have to overcome the inherent non-uniqueness of any potential field method (Blakely, 1995).

~~As oceanic lithosphere corresponds to the top boundary layer of mantle convection, its fine-scale structure attests to a variety of dynamical processes~~ Additionally, in~~the mantle, and delineating it would bring to a better understanding of geodynamics and mantle rheology. Two main lithospheric cooling models have been produced to explain the observations of decreasing heat flux and increasing depth with age. In the oceanic plate model (McKenzie, 1967, Stein and Stein, 1992), the mature lithosphere reaches a limiting thickness, after which it ceases to cool and acts as a steady-state conducting layer, with a lower boundary maintained at a fixed temperature by contact with the asthenosphere. On the other hand, with the cooling half space model, which includes boundary conditions to account for the evolution of latent heat where the plate is growing (Parker and Oldenburg, 1973), the lithosphere continues to increase in thickness with age. However, the reason for the apparent shallowing of the ocean floor which is older than ca. 80 Ma is still an open issue, which the cooling models are not able to explain, and the quality of observations is not~~

~~sufficient to unravel.~~

~~On the basis of the surface wave tomography of the Pacific mantle, Ritzwoller et al. (2004) have suggested that old lithosphere does not follow half-space cooling, however the spatial resolution of their tomography does not enable them to rule out that there may be a flattening effect of hotspot chains and oceanic plateaus.~~

~~In~~ gravity analyses, errors can occur if internal boundaries (chemical or phase) with density contrasts, or the Earth's viscosity structure are not appropriately considered~~. If~~: if a low viscosity zone lies between an upwelling mass and the Earth's surface, the rising mass will then be relatively inefficient at warping the surface and will be largely compensated for from below, through the deformation of deeper density discontinuities (Mc Nutt, 1998).

An ~~integrated tomography~~attempt to integrate seismological and gravity observations in the Pacific area is given by the global model of Simmons et al. (2010~~)~~), which simultaneously considered seismic observations and a large suite of convection-related geodynamic constraints to obtain a three-dimensional (3-D) model of mantle density, shear wave speeds, and compressional-wave speeds. The results enabled Simmons et al. (2010) to simultaneously reconcile dynamic topography and gravity, to a wide extent (72%). They succeeded in distinguishing the thermal from the compositional contribution to both seismic velocities and densities. However, the resolution of the model is still not sufficient for continental studies (approximately 2.5° x 2.5° x 75 to 240 layer thickness). In terms of the Pacific Plate, the model does not discriminate the boundary layer between the lithosphere and the asthenosphere, which could help to resolve what happens to lithosphere plates older than 80 Ma.

In this paper we test the possibility of using integrated approaches, which

Formatted: Space After: 12 pt, Don't add space between paragraphs of the same style

consider both seismic and gravity constraints, in order to recover a high-resolution ~~3D~~3-D density model of the upper mantle and the lithosphere of the Pacific Region, with a lateral resolution of 1° x 1°, down to a 300 km depth and use it as a proxy for dynamic topography.

Density anomalies are recovered using the inversion approach of Sequential Integrated Inversion (SII; (Tondi et al., 2000)), which has ~~recently~~ been parallelized to allow for a large data set and a large number of parameters (Tondi et al., 2012). We ~~apply this approach to~~specify an initial mean 1-D density model within a volume of 179° x 177° x 300 km that is updated to a 3-D density model (179 x 177 x 17 model parameters) through the combined use of the surface waveform tomography of the Pacific upper mantle (Maggi et al., 2006) and ~~the first~~a gravity model from the ESA Earth's explorer GOCE (Gravity -field and Ocean Circulation Explorer) mission (Drinkwater et al., 2003). ~~In what follows, we first explain how to obtain~~Assuming that the ~~density model from~~Earth's lithosphere is the ~~inversion procedure. We then describe how~~upper cold thermal boundary layer of a convecting system, the thickness of the lithosphere in our model is determined with Müller et al., (2008) isochrons and, where this information is not available, or is in contrast with the above physical assumption, we assign the depth where we observe a decrease in the depth-density curve of our final 3-D density model (hereinafter referred to as SII-ρ). The gravity field ~~produced by~~calculated for the ~~3-D density~~ SII-ρ structure, -limited to the depth of the lithosphere, enables us to recover both the residual topography and the mantle residual gravity anomalies. Finally, we show that an estimation of the correlation matrix between the residual topography and the mantle residual gravity anomalies gives a proxy of the regions where the

Formatted: Indent: First line: 1.25 cm

~~sublithospheric mantle density contributes to surface topography~~convective circulation of the sublithospheric mantle contributes to surface topography. In order to observe the added value of our approach, results obtained with the SII-ρ structure and those recovered from the density model, directly converted from seismic data are compared. The *a posteriori* standard deviation associated with the updated density parameters enables the reader to quantify the reliability of the results. Additionally, a fully 3-D map of the ρ-v_{SV} scaling relationships will help to better understand and interpret the interplay among the geodynamic features and processes that occur beneath and on top of the Pacific Plate.

2. DATA AND METHODS

2.1. The gravity database

The GOCE mission provides independent estimates of the Earth's gravitational field, thus improving the present knowledge of low and medium frequencies and reducing systematic effects (bias and trend) at a local scale. To obtain free-air gravity anomalies from the GOCE mission data, we used the fourth release of the time-wise spherical harmonic expansion (Pail et al. 2011). This is a GOCE-only solution (no GRACE data are included) complete up to degree and order 250. The global commission error at this maximum degree is 3.93 mgal (Figure 1), while the omission error computed from EGM2008 degree variances (Pavlis et al. 2012) is 13.77 mgal. Consequently, the GOCE-only solution is combined with the EGM2008 ultra-high resolution global gravitational model, which is also based on ground and altimetry data, as well as a GRACE model (Mayer-Gürr 2006). Details on the combination weighting strategy, which is only driven by the

coefficient error variances, are given in Gilardoni et al. (2013). Using this model the commission error up to the maximum degree of 2190 is about 4.01 mgal, as the omission error is practically negligible.

Once the spherical harmonic coefficients have been chosen and the contributions of the normal potential have been removed (Heiskanen and Moritz 1967), free-air gravity anomalies in spherical approximation are computed by a classical synthesis operation, i.e.

$$\Delta g(\varphi,\lambda,r) = \frac{GM}{R^2}\sum_{n=2}^{N}\left(\frac{R}{r}\right)^{n+2}(n-1)\sum_{m=-n}^{n}T_{nm}Y_{nm}(\varphi,\lambda) \quad (1)$$

$$\Delta g(\varphi,\lambda,r) = \frac{GM}{R^2}\sum_{n=2}^{N}\left(\frac{R}{r}\right)^{n+2}(n-1)\sum_{m=-n}^{n}T_{nm}Y_{nm}(\varphi,\lambda) \quad (1)$$

where (φ, λ, r) are the spherical coordinates of grid points over the reference ellipsoid, GM is the gravitational constant by the Earth's mass, R is a reference Earth radius, Y_{nm} are the spherical harmonics of degree n and order m, and T_{nm} are the coefficients of the series truncated at the maximum degree N. A map of the computed gravity anomalies from the combined GOCE-EGM2008 model is shown in Figure 32(a).

The availability of a topography/bathymetry dataset in resolutions up to 1 arc minute (ETOPO1, Amante and Eakins, 2009) enables us to calculate the Bouguer gravity map with a Bouguer density correction of 2670 kg/m^3 on land and a correction of -1640 kg/m^3 to correct for bathymetry (Caratori Tontini et al. (2007)). The Bouguer gravity anomalies, shown in Figure 32(b) are used as gravity observations for the optimization of the density parameters. On the basis of the estimated commission error, the a-priori gravity data error is set at 4.0 mGalmgal for all the measurements (the square root of the diagonal elements of

Formatted: Indent: First line: 1.25 cm

Formatted: Lowered by 14 pt

Formatted: Lowered by 14 pt

Formatted: Indent: First line: 1.25 cm

$\mathbf{C}_{gg}$).

2.2. Design of a 3-D density model

~~Our integrated approach~~The Sequential Integrated Inversion (SII, Tondi et al., 2012) involves finding the maximum of a likelihood function (L) that relates density ~~earth~~Earth structure (ρ) to our gravity observations (**g**) and our seismic velocity structure (**v**) through three types of information: ~~-~~(i) gravity data, (ii) information from the analysis of a seismological data-set ($\Delta\boldsymbol{v}$), and the (iii) information on the physical correlation between the density and the velocity parameters (α, C_{mm}):

$$L\text{~~}(dg, d\rho, dv)\text{~~}(\Delta\boldsymbol{g}, \Delta\rho, \Delta\boldsymbol{v}) = exp\text{~~}\left\{-\frac{1}{2}[dg - Gd\rho]^T C_{gg}^{-1}[dg - Gd\rho]\right\}\text{~~}\left\{-\frac{1}{2}[\Delta\boldsymbol{g} - G\Delta\rho]^T C_{gg}^{-1}[\Delta\boldsymbol{g} - G\Delta\rho]\right\} x\ exp\text{~~}\left\{-\frac{1}{2}[d\rho - \alpha dv]^T C_{mm}^{-1}[d\rho - \alpha dv]\right\}\text{~~}\left\{-\frac{1}{2}[\Delta\rho - \alpha\Delta\boldsymbol{v}]^T C_{mm}^{-1}[\Delta\rho - \alpha\Delta\boldsymbol{v}]\right\} \quad (2)$$

The resulting SII algorithm allows the iterative estimation of the update (Δρ) to the starting density model (ρ_0):

$$\Delta\boldsymbol{\rho} = (\mathbf{G}^T\mathbf{C}_{gg}^{-1}\mathbf{G} + \mathbf{C}_{mm}^{-1})^{-1}(\mathbf{G}^T\mathbf{C}_{gg}^{-1}\Delta\mathbf{g} + \alpha\mathbf{C}_{mm}^{-1}\Delta\mathbf{v})\text{~~}\text{□□□}) \quad (3)$$

where **G** is the matrix of the partial derivatives of the gravity observations (**g** = [g_1, g_2, …g_N], n ∈ [1,N]) ~~relative~~with respect to the density model parameters ($\rho^{(i)}$ = [ρ_1, ρ_2, … ρ_M], m∈ [1,M]), $\mathbf{C}_{gg}$ is the square diagonal covariance matrix of the gravity data uncertainties, ~~-~~$\mathbf{C}_{mm}$ is the covariance matrix that takes ~~in~~into account the error propagation from the velocity to the density model, $\Delta\mathbf{g}$ = ($\mathbf{g}^{OBS}$ – ~~$\mathbf{g}^{(i)}$~~)~~$\mathbf{g}^i$~~) the i-th model predicted gravity response~~),~~ α = [α_1, α_2, …α_M], m∈ [1,M] the velocity-density gradient vector, in the same parametrization as the model, $\Delta\mathbf{v}$ =

Formatted: Indent: First line: 1.25 cm

Formatted: Font: Bold

Formatted: Font: Bold

($\boldsymbol{v}$ - $\boldsymbol{v}^0$), the velocity parameter adjustment vector of dimension M.

The flow chart in Figure ~~2,~~3 schematically summarizes the processing steps of the inversion procedure. ~~Accordingly~~According to Maggi et al., (2006), our starting velocity model ($\boldsymbol{v}^0$) is the superposition of the average crustal part of the 3SMAC (Nataf and Ricard, 1996) 3-D ~~earth~~Earth model and the smoothed version of the ~~1D~~1-D $\boldsymbol{v}_{SV}$ profile from PREM (Dziewonski and Anderson, 1981). The model covers the whole Oceanic plate (90°N 90°S) (121°E 60°W) up to a depth of 400 km and is parametrized with a rectangular grid with a spatial resolution of 1° x 1° x 17 layers of variable depth.

The ~~first (i=1)~~ seismic update (~~$\Delta \boldsymbol{v}$~~)$\Delta \boldsymbol{v}^0_{SV}$) is recovered from the regional surface waveform tomography of the Pacific upper mantle, obtained using an automated multimode surface waveform inversion technique on fundamental and higher mode Rayleigh waves (Maggi et al., 2006). Considering the proved relationships between the isotropic shear-wave velocity and the density parameters [Kozlovskaia et al., 2004), only the isotropic shear-wave speeds have been considered. ~~Contextually,~~

With regard to the starting density model (ρ^0), it is obtained from the starting velocity model ($\boldsymbol{v}^0$) ~~is transformed into the starting density model (ρ_0)~~ through an *a* ~~ρ-v_S~~*priori* v_{SV}-ρ depth-dependent relationship. In order to ensure the optimum choice of physical relationships between the seismic velocities and bulk densities:

1. We assume a node-dependent linear relationship: $\rho_m = \alpha_m v_m + \beta_m$, i.e. with a-priori information~~,~~ we can use different relationships (correlation coefficients α and β) for different model parameters; hence a fully 3-D ρ–v_S scaling relationship;

Formatted: Superscript

Formatted: Superscript

Formatted: Superscript

Formatted: Font: Italic

Formatted: Subscript

2. Through a slight modification of equation (3), the gradient of the relationship, α, is now inverted and optimized independently for each model parameter:

$$\alpha_m = (\mathbf{G}^T C_{gg}^{-1} \mathbf{G}(\boldsymbol{v}^0 + \Delta v_m))^{-1} (\mathbf{G}^T C_{gg}^{-1} \mathbf{g}) \quad (4)$$

3. The $\mathbf{C}_{mm}$ matrix takes into account the error propagation from the velocity to the density model:

$$\sigma(\boldsymbol{\rho}_m) = \boldsymbol{v}_m \sigma(\alpha_m) + \alpha_m \sigma(\boldsymbol{v}_m) + \sigma(\beta_m) \quad (5)$$

where $\sigma(\boldsymbol{v}_m)$ is the seismic *a priori* model variance (0.05 km s^{-1}), weighted with the standard deviation associated with the path-averaged velocities, $\sigma(\alpha_m)$ and $\sigma(\beta_m)$ are the uncertainties in the coefficients of the scaling $\boldsymbol{\rho}_m$-$\boldsymbol{v}_m$ relationship. To control the amount of variation and to allow for correct changes in the parameter values, various tests were performed through the optimization process. The values on the main diagonal of $\mathbf{C}_{mm}$ (under the assumption that there is no correlation between the errors in each node) are chosen for an optimum trade-off between the data variance and the solution variance. Very small values of $\mathbf{C}_{mm}$ correspond to high values of C_{mm}^{-1}, hence representing over-regularized solutions where the density model remains close to the seismic model. Taking into account the *a posteriori* seismic ~~model resolution~~standard deviation matrix (in Figure 4 (a) are shown the mean diagonal elements); extensively analyzed in Maggi et al., ~~[~~2006~~]),).~~ higher $\sigma(\alpha_m)$ and $\sigma(\beta_m)$ uncertainties are assigned below a depth of 200 km~~.~~ (Figure 4 (b)). This enables the complementarity of the seismological and gravity data sets to be exploited, and reliable solutions to be obtained also below the seismic

Formatted: Superscript

Formatted: Superscript

depth resolution.

~~For~~As for our initial ~~ρ-v_{SV}~~ $v^0_{SVm} - \rho^0_m$ relationship, we use a scaling profile derived from the empirical Birch's law (Birch, 1964). The widespread success of Birch's law can be ascribed to its virtual coincidence with, and hence linearization of, a power law derived from lattice dynamics over the density range ≈2.5–4.0 g/cm^3 (Chung, 1972), within which ~~is typical of~~ the ~~rock~~rocks and minerals vary in our model. In addition, for our depths, the general trend of the pyrolite models (Cammarano et al., 2005), which are the best approximation of the composition of the Earth's upper mantle, does not differ much from the trend of the 1-D Birch relationship. Birch's law concerns P-wave velocities; our ~~ρ-v_{SV}~~ $v^0_{SVm} - \rho^0_m$ depth-dependent relationships are the regression lines drawn through the plot of the two variables extracted from his tables. However, as studied by Simmons et al., (2009), a simple 1-D velocity-density scaling implies a direct relationship among seismic velocities, temperatures and density material. As this simplified view of density heterogeneity is clearly not correct, to account for additional dependencies on a wide range of factors, such as the presence of fluids or compositional variations, we allow the density-velocity scaling to vary laterally during the inversion, through (4), thus creating a fully 3-D relationship between the density and the shear-wave velocity model.

To proceed with the SII, we use the ~~transformed~~ 3-D grid of our starting density ~~values in the Earth's volume of 178° x 176° x 300 km~~model (ρ^0_m) to calculate the predicted gravity response **g** and the partial derivatives of each gravity measurement $\mathbf{g}_n$ (where n are the [1,N] gravity observations) with respect to each density model parameter ρ_m: ~~$\mathbf{G} = \left[\left(\frac{\partial g_n}{\partial \rho_m}\right)_{n,m}\right]^{N \times M}$ (6)~~

Formatted: Superscript

Formatted: Not Superscript/ Subscript

$$\mathbf{G} = \left[\left(\frac{\partial g_n}{\partial \rho_m}\right)_{n.m}\right]^{NxM} \quad (6)$$

Residuals between the observed (Fig. 2 (b)) and the calculated gravity field ($\Delta\mathbf{g}$) are used as input for the inversion algorithm in (3). We then optimize the starting density-~~v_S~~v_{SV} scaling relationships ~~(α_m)~~ (α_m^0) and the starting density values ~~(ρ_m)~~ (ρ_m^0), with (α_m^1) and $\Delta\rho_m^1$ (Figure 4 (c)) respectively.

At the same time, we calculate the gravity data misfit and the *a posteriori* standard deviation associated with the updated density parameters. The gravity data misfit is expressed as the *rms* of the gravity residuals for each observation:

$$rms = \sqrt{\frac{\sum_{i=1}^{N}(g_i^{obs} - g_i^{calc})^2}{N}}\sqrt{\frac{\sum_{n=1}^{N}(g_n^{obs} - g_n^{i})^2}{N}} \quad (7)$$

where $(g_n^{obs} - g_n^i)$ is $\Delta\mathbf{g}$, as expressed above.

The *a posteriori* standard deviation, associated with the updated density parameters, $(\rho_m^i = \rho_m^{i-1} + \Delta\rho_m^i)$, is calculated as:

$$\sigma\rho_m = \alpha_m \sigma v_{SM} \rho_m^i =$$

$$\alpha_m^i \sigma v_{SVm}^{i-1} \left[1 - \left(Var(g(n)) \frac{d_{mm}}{max\,(d)}\right)\right]\left[1 - \left(Var(g(n)) \frac{d_{mm}}{\max\,(d_{mm})}\right)\right] \text{ (m=1,...M)}$$

(i=the current iteration) (8)

which is the propagation of uncertainty from the velocity- to the density model, weighted with the final gravity variance reduction Var(g(n)), and the information provided by the gravity data (d_{mm} the diagonal elements of the gravity kernel $(G^T C_{gg}^{-1} G)$). -The procedure is repeated, following the flow chart in Figure ~~2~~3, until a satisfactory fit to the observed datasets (data misfit) is achieved~~(~~. The higher the uncertainty in the input information, the lesser the number of iterations needed to obtain a model that satisfies both the datasets (however,

Formatted: Left, Indent: Left: 6.24 cm, First line: 1.25 cm

usually not more than 2–3 iterations).

2.3. Residual topography and mantle residual gravity anomalies

To recover the residual topography, the effects of the isostatic lithosphere are estimated with Panasyuk and Hager's (2000) algorithm and subtracted from the observed elevation (ETOPO1, Amante and Eakins, 2009). We assume that isostatic compensation is achieved within the lithosphere. Isostatic compensation can be achieved because both continental and young oceanic lithosphere essentially floats (mature oceanic lithosphere becomes increasingly denser than the asthenosphere and eventually sinks at subduction zones) on a relatively inviscid substrate (viscosity ~~of~~ one order of magnitude lower than that of the upper mantle~~).~~), i.e. the weak peridotite of the asthenosphere (Zhou, S., and Sandiford, M., 1992). Changes in the buoyancy or elevation of the lithosphere are accommodated by the displacement of the asthenospheric mantle in a finite length of time, related to its effective viscosity~~. The rebound following the removal of the Pleistocene Laurentide icecap shows that the time scales appropriate for this isostatic response are of the~~ , in the order of 10^4-10^5 years. The ~~existence~~association of ~~large lateral temperature gradients in~~ the ~~oceanic~~Earth's lithosphere ~~leads to significant horizontal density gradients. These thermally-induced density changes lead to corresponding changes in the surface elevation of the oceanic lithosphere, through a kind of~~with the upper cold thermal ~~isostasy. In order to identify~~boundary layer of a convecting system (Schubert et al., 2001) enables us to select the depth of the lithosphere in our SII-ρ model~~,~~. For each 1-D *xy* density depth profile we consider ~~Müller~~the depth recovered from Muller et al., ~~(1997) isochrons~~(2008) isochrones as a guide, and~~,~~

Formatted: Indent: First line: 1.25 cm

~~where this information is not available,~~ we opportunely adjust the value in order to assign ~~the~~a depth point where we observe ~~a decrease~~an inversion in the ~~depth-velocity curve of our final 3-D density model (hereinafter referred to as SII-ρ).~~density gradient.

The mantle residual gravity anomalies are estimated as the differences between the gravity field produced by SII-ρ limited to the depth of the lithosphere and the observations.

~~An estimation of~~Following the steps sketched in Figure 5, we estimate the correlation matrix between the residual topography and the mantle residual gravity anomalies ~~gives~~. We believe that a graphical representation of the diagonal values of this correlation matrix may be a proxy of the regions where the sublithospheric mantle density contributes to surface topography. We base our assumption on the papers of Pekeris (1935) and Richards and Hager (1984), which have shown that the viscous mantle flow that is driven by the thermal density contrasts is responsible for the long-wavelength gravity anomalies observed at the surface. They demonstrated that the gravitational effects of surface deformation caused by the thermally driven flow is opposite in sign and comparable in magnitude to that of the driving density contrast. It is therefore reasonable to expect that sublithospheric density contrasts have effects on the surface topography if a negative correlation is found between the residual topography and the mantle gravity residuals. This means that we can rule out compensations due to a low viscosity region at the base of the lithosphere.

Formatted: Indent: First line: 1.25 cm

3. RESULTS

Depth sections of the resulting SII-ρ density model, up to 300 km, after the

Formatted: Indent: First line: 1.25 cm

first iteration, are plotted in Figure ~~4 (a) as a percentage deviation with respect to the mean model of each layer (Figure 4 (b)). The gravity data field reproduced by the resulting density model is shown in Figure 5. We obtain a gravity data misfit of 66.73 mgals (with respect to 321.16 mgals of the seismological model scaled into a density model) and a data variance reduction of 67.41% (with respect to 0.32% of ρ_0). The *a posteriori* standard deviation (Figure 6), associated with the density parameter, ranges between 2.6 and 75.4 kg/m^3.~~ 6 (a) as a percentage deviation with respect to the mean model of each layer (Figure 6 (b)). ~~Further iterations do not improve the results, while they decrease the fit to the seismological data.~~

The optimization of the ρ-v_{SV} correlation coefficient in □3□□□enabled us to obtain the 3-D map of lateral variations in the angular coefficients of the ρ-v_{SV} coupling with respect to the 1-D thermal relationships (temperature variations are the dominant cause of density variations), and to select the regions characterized by density compositional signatures (Simmons et al., 2010, Tondi et al., 2012b). Figure 7 shows our interesting results. First of all compositional variations presumably only affect to densities at the lithosphere-asthenosphere boundary (LAB), as chemically-induced density anomalies show up gradually from the Eastern to the North Western Pacific plate and do not extend below 200 km in depth. Additionally, important anomalies are observed mostly west of the East Pacific Rise (EPR) and are particularly emphasized at depth, beneath the northwestern part of the lithosphere.

The gravity data field reproduced by the resulting density model is shown in Figure 8. We obtain a gravity data misfit of 66.73 mgal (with respect to 321.16 mgal of the seismological model scaled into a density model) and a gravity data

variance reduction of 67.41% (with respect to 31.58% of the seismic model). A comparison between the observed (Fig. 2 (b)) and the reproduced gravity data field (Fig. 8) evidences a good reproduction of the pattern of the Bouguer anomalies, with a uniform underestimation of densities within the Pacific Plate that is probably explained by the uncertainties in the recovered ρ-v_{SV} relationship (Figure 9) and that cannot affect our next inferences.

The *a posteriori* standard deviation, associated with the density parameters (Figure 10), ranges between 2.6 and 75.4 kg/m^3. Higher reliability of the density model, associated to smaller values of standard deviation, is obtained within the Pacific Plate, from 100 to 200 km depth. Further iterations do not improve the results, while they decrease the fit to the seismological data.~~The SII-ρ model produces nonisostatic topography characterized by general positive values in the Pacific plate, which generally increase on the north-western side and reach up to +5 km in the North West Pacific basin and in the Philippine Sea. Important positive values are found along the East Pacific Rise. On the other hand, continental regions are overcompensated.~~

~~The~~

The identified thickness of the isostatic lithosphere in the Pacific plate ranges from 8 km in the EPR to 120 km depth in the Philippine Sea (Figure 11 (a), (b), (c)), including about 11 layers of the SII-ρ model.

The possibility to have available density information every 1°, enabled us to use detailed density profiles to calculate a) the differences between the produced gravity field of the 3-D lithospheric density structure and the observations, i.e. the mantle residual gravity~~, show a strong negative mantle gravity anomaly characterizing~~ and b) the ~~whole Pacific plate, which is correlated~~isostatic height

Formatted: Font: Cambria

Formatted: Font: Cambria

to ~~positive~~ be subtracted from topography ~~residuals.~~

~~We test~~/bathymetry. Hence, we have tested the sensitivity of both the calculated ~~residual topography and the~~ mantle residual gravity anomalies~~,~~ and the residual topography to (~~1~~i) the lithosphere depth uncertainty~~,~~ derived from the provided standard deviation associated with the Müller et al., (~~1997~~2008) isochrones, and to (~~2~~ii) the chosen density model ~~(~~: the SII-ρ model (Figure 6 (a)) and the seismological velocity model transformed into a density model through the initial ρ-v_{SV} depth-dependent relationship~~).~~.

The mantle residual gravity related to the SII-ρ model (Figure 11 (d), (e), (f)), shows a negative anomaly characterizing the whole Pacific plate with a gradient of 500 mgal between the eastern and the western coast. With regard to the SII nonisostatic topography (Figure 11 (g), (h), (i)), it is characterized by general positive values in the Pacific plate, which generally increase in the north-western side and reach up to +3 km in the North West Pacific basin and in the Philippine Sea. Important positive values are also found along the EPR. On the other hand, continental regions are overcompensated.

Our sensitivity analysis shows that the variation in the depth of the lithosphere (Figure ~~7~~11 (a), (b) and (c~~)),~~)), as expected, particularly affects the residual gravity, by lowering or increasing the mantle gravity residual anomalies (Figure ~~7 (d), (e), (f) and Figure 8 (a), (b), (c)). The~~11 (d), (e), (f)): a thinner lithosphere results in higher residual gravity anomalies. On the other side, the residual topography associated with the Pacific plate (Figure 11 (g), (h), (i)) is slightly affected by the uncertainty associated with the depth of the lithosphere, but the range of variations of the anomalies is more important when considering a thicker lithosphere (Figure ~~7~~11 (i~~), Figure 8 (f~~)).

Formatted: Font: Cambria

~~We observe more positive mantle~~Mantle gravity residuals ~~with~~expressed by the SII-ρ ~~density~~ model (Figure ~~7~~12 (d), (e), (f)), are generally more negative with respect to ~~the model, directly transformed from~~ those produced by the seismological model ~~with the Birch relationship.~~(Figure 12 (a), (b), (c)). Therefore this implies that SII-ρ ~~density~~ model has a ~~lighter~~denser lithosphere~~.~~ ~~Conversely, on the side of the~~, density increasing with depth, with a Δρ from 40 to 170 kg/m^3. As a consequence, residual topography~~, there is a stronger positive signal for~~ associated to the seismic model ~~converted into a density model~~ (Figure ~~8~~12 (d), (e), (f~~)).~~)) shows a stronger positive signature with an average Δh of 1.5 km.

The analysis of the negative correlation between the residual topography and the mantle residual gravity~~,~~ which, following Pekeris (1935) and Hager et al., (1985), should ~~be a proxy for~~identify the regions where the contribution of mantle circulation in supporting the long-wavelength topography~~,~~ is active, enabled us to draw the pictures shown in Fig. ~~9~~13 (a) to (f~~)~~), for both the seismic and SII density models. Correlation is calculated for the *xy* grid of the 3-D model as:

$$d_p = \frac{(h_{res} - (\overline{h_{res}} + \sigma(h_{res}))}{(g_{res} - (\overline{g_{res}} + \sigma(g_{res}))} \quad (9)$$

where h_{res} is the residual topography and g_{res} is the mantle residual gravity, both weighted over the mean ($\overline{h_{res}}$ and $\overline{g_{res}}$) and the standard deviation ($\sigma(h_{res})$ and $\sigma(g_{res})$) in order to be comparable quantities. Fig. 5 shows the main steps we have followed to obtain our results.

~~The proxies of dynamic topography are also tested with respect to~~As shown in Figure 13, the ~~lithosphere depth uncertainty and to the chosen~~ density model~~.~~ ~~The density model~~ used in the calculation of (9) has a ~~larger~~significant impact in

determining the ~~amplitude~~width of the area of the Pacific region affected by dynamic topography. If we use the density model~~,~~ directly transformed from the seismic model, the influence of mantle flow on the surface topography ~~(Fig. 9 (a), (b), (c)) is extended~~extends from the Peru-Chile trench to the Tonga trench in the South Pacific and from the west coast of the USA to the Philippine Sea in the North Pacific~~.~~ (Figure 13 (a), (b), (c)). On the other hand, if we use the ~~density~~SII-ρ model ~~recovered from,~~ the ~~combined inversion of seismological and gravity data, the~~estimated contribution of mantle flow to the surface bathymetry ~~(Fig. 9 (d), (e), (f))~~ is limited mostly to the eastern side of the Pacific plate~~,~~ (Figure 13 (d), (e), (f)), and is more consistent with the ~~features of the~~ geoid ~~height (Fig. 10~~lows (Figure 14). In addition, the ~~two models show a different contribution of~~lithospheric depth uncertainties contribute in enlarging (when the lithospheric depth is smaller) or reducing (when the lithospheric depth is greater) the ~~residual~~region affected by dynamic topography ~~and the mantle residual gravity to (9).~~.

We wish to note that our results rely on a starting tomography model (Maggi et al., 2006) which is undoubtedly limited by both spatial resolution and the used methodology. However, as studied in Tondi and de Franco (2006), the interplay with gravity information ~~constrains the result,~~can efficiently constrain and complete the seismic information. Additionally, the methodology enables us, through an assessment of the gravity residuals ~~enables us,~~ to become aware of the model inconsistencies ~~and of under- or over-estimated densities. A comparison between the observed and the~~ . As evidenced above, gravity residuals reproduced ~~gravity data field evidences only~~by SII-ρ model show a slight uniform underestimation of densities ~~below~~beneath the Pacific Plate, that

do not alter the ~~oceanic crust, which is probably due to~~interdipendence among the ~~uncertainties in~~different regions of the ~~recovered ρ-v_S relationship~~model, and ~~that cannot affect~~as a consequence, our inferences.

4. DISCUSSION

4.1 The SII density model of the Pacific lithosphere and upper mantle

~~The recovered SII density values plotted against the seismological shear velocities (~~The most prominent large-scale feature of the shallower pattern of density anomalies, up to 150 km in depth (Figure 6 (a)), is a progressive increase in density values across the Pacific plate from East to West, consistent with the lithospheric age (Muller et al., 2008). At depth, as visualized with the help of density isosurfaces (Figure 15), the high density/velocity anomaly reduces and is gradually replaced by a uniform lower density anomaly which encompasses the subsurface of all the plate. The reliability of these results is supported by the calculation of the *a posteriori* standard deviation associated with the density parameters (Figure 10), which evidences an excellent anomaly recovery in the Pacific plate between depths of 100 and 200 km, where the model is well constrained by both seismological and gravity information. This enables us to evaluate, with confidence within that depth interval, both the recovered density parameters and the deviation of the optimized angular coefficient of the ρ-v_{SV} relationship, with respect to the a priori Birch coefficient.

Within the lithospheric depth, the progressive reduction of the positive density anomaly (Fig. 6 (a)) correlates well with the increase of a chemically-induced density anomaly (Fig. 7), which at 150 km depth becomes particularly

important beneath the northwestern part of the lithosphere and may help to explain some inconsistencies between geodetical and seismological observations. In fact, almost all seismological studies (Forsyth, 1977, Zhang and Tanomoto, 1991, Maggi et al., 2006) show that lithospheric seismic velocities, the thickness of the seismic lithosphere and the seismic velocities, in the low-velocity zone below the lithosphere, all increase continuously with age when averaged over isochrons, and do not flatten out for older lithosphere in the same way that geoid and gravity observations do. ~~Fig. 11) enable us to analyze the new density-v_s scaling relationships and compare them to the initial Birch relationship. It should be noted that the general trend of the SH ρ-v_s~~Thus, the non-thermal density anomalies at the base of the lithosphere may reduce the weight of the lithosphere in that part of the model and explain the modest impact on the gravity and geoid measurements.

Mid-ocean ridges, the western and the southern parts of North America continent and the central Australian Proterozoic region below the Alice Springs Orogeny (Kennett and Iaffaldano, 2013) are characterized by negative density anomalies. Unlike the results of the tomographic inversion (Maggi et al., 2006), and in line with Dunn and Forsyth (2007), the negative density anomaly beneath the EPR is only slightly visible at shallower depths, becoming important between 200 and 250 km and disappearing at 300 km, thus confirming that convection is largely driven by cooling from above. No compositional contribution is observed from the analysis of the ρ-v_{SV} angular coefficient (Fig. 7), thus indicating that all anomalies are thermally induced heterogeneities. Positive density anomaly structures separated by negative density anomalies characterize the subsurface of convergent plate boundaries (Aleutian Trench, Mariana Trench, Kuril Trench,

Formatted: Font color: Auto

Formatted: Indent: First line: 1.25 cm

Kermadec Trench) and the subduction zones of Japan and Tonga-Kermadec, down to a depth of 300 km and below. The negative density anomalies probably reflect upward intrusions of arc magmas and/or fluids from hydrous partial melts in the mantle wedge. This is justified by the fact that the fluids control the pore fluid pressure and thus play an important role in the nucleation of interplate megathrust earthquakes, as well as large crustal earthquakes, which are typical in the arc and backarc areas (Zhao et al., 2002). At a depth of 200 km and below, positive density signatures of the continental cratons of Australia and North America are clearly visible.

In order to have a comprehensive insight of the contribution of the compositional heterogeneities to the overall density field of the Pacific plate, and extrapolate the contribution of the gravity data to the seismic model, the recovered SII density values have been plotted against the seismological shear velocities (Figure 9). It is evident that the general trend of the SII ρ-v_{SV} relationships follows the 1-D Birch relationships, which is the same as the general agreement between the upper mantle density anomalies and the velocity structures observed by the tomographic inversion of Maggi et al., (2006). However~~, on the basis of the assigned covariance matrix~~, the SII optimization procedure increases the value of the a priori α coefficient (the gradient of the ρ-v_{SV} relationship), within the limits of 10% - 40~~%. Lower values are assigned~~% that, with the help of Figure 7, we localize to the parameters that belong to the ~~continent and higher values to the~~ oceanic lithosphere and to the upper mantle structures below the ~~oceanic~~Pacific plate. ~~As a result of the general increase in density parameters related to the area of the oceanic plate, our 1D mean density model, unlike the starting 1D v_s model (Figure 2 in Maggi et al., 2006), is higher~~

~~than PREM between 50 and 220 km (Fig. 4 (b)).~~ These results are consistent with the findings of Simmons et al., (2009) of a positive residual density anomaly beneath the eastern Pacific Ocean extending from Antarctica to Alaska, which does not have a thermal origin. ~~Additionally, as~~ Lowered scaling factors are observed ~~by Ekström~~within and ~~Dziewonski (1998),~~below the ~~presence~~continental lithosphere, but in this case, higher values of ~~an underestimated radial anisotropy anomaly beneath~~ the ~~Pacific plate leads~~a posteriori standard deviation suggest us to ~~differences between the V_S profiles of two groups of data: one consisting of observations~~evaluate this result with ~~primary sensitivity to v_{SH} (for example, Love waves), the shear wave velocity of a transversely polarized horizontally travelling S wave, which remain close to the PREM values, and the other consisting of observations sensitive to v_{SV} (for example, Rayleigh waves), the velocity of a vertically travelling S wave, which are significantly more positive~~caution.

~~The most prominent large-scale feature of the shallower pattern of density anomalies, up to 150 km in depth, is a progressive increase in density values across the Pacific plate from East to West, consistent with the lithospheric age. At depth, as visualized with the help of density isosurfaces (Figure 12), the low density/velocity area expands and encompasses the subsurface of all the plate.~~

~~Mid-ocean ridges, the western and the southern parts of North America continent and the central Australian Proterozoic region below the Alice Springs Orogeny (Kennett and Iaffaldano, 2013) are characterized by negative density anomalies.~~ ~~Unlike the results of the tomographic inversion, and in line with Dunn and Forsyth (2007), the positive density anomaly beneath the East Pacific Rise is only slightly visible at shallower depths, becoming important between~~

~~200 and 250 km and disappearing at 300 km. Positive density anomaly structures separated by negative density anomalies characterize the subsurface of convergent plate boundaries (Aleutian Trench, Mariana Trench, Kuril Trench, Kermadec Trench) and the subduction zones of Japan and Tonga-Kermadec, down to a depth of 300 km and below. The negative density anomalies probably reflect upward intrusions of arc magmas and/or fluids from hydrous partial melts in the mantle wedge. The fluids control the pore fluid pressure and thus play an important role in the nucleation of interplate megathrust earthquakes, as well as large crustal earthquakes in the arc and backarc areas (Zhao et al., 2002).~~

~~At a depth of 200 km and below, positive density signatures of the continental cratons of Australia and North America are clearly visible.~~

~~The *a posteriori* standard deviation (Figure 6), associated with the density parameters, highlights the reliability of seismic analysis: poor at the north-eastern and southern side of the semiglobe and generally good in the Pacific plate, and of the gravity sensitivity kernels, which are more informative between depths of 100 and 200 km.~~

As a result of the general increase in density parameters related to the area of the Pacific plate, our 1-D mean density model, unlike the starting 1-D ρ model directly transformed from seismic data, is higher than PREM between 50 and 220 km (Fig. 6 (b)). The contribution of gravity information, may have corrected the density values that are linked to observations with primary sensitivity to v_{SV} (e.g. the Rayleigh waves) that, as observed by Ekström and Dziewonski (1998), in the presence of an underestimated radial anisotropy anomaly beneath the Pacific plate, are of significant smaller amplitude, with respect to parameters obtained from observations with primary sensitivity to

Formatted: Indent: First line: 1.25 cm

641 v_{SH} (e.g. Love waves).

642

643 *4.2. The*

644 ~~*4.2. The residual topography and the*~~ *mantle residual gravity anomalies and the*

645 *residual topography of the Pacific Plate*

646 As discussed in ~~the Introduction,~~McNutt (1998), the high viscosity of the

647 plates ~~shields~~may shield surface geologic processes from convective forces

648 below ~~(Mc Nutt, 1998).~~and explain the deviations of ocean depth or seafloor

649 topography from the prediction of a cooling half-space model. As a result, the

650 residual topography~~,~~ (Figure 11 (g), (h), (i) and Figure 12 (d), (e), (f)), which is

651 estimated on the basis of the ~~properties of~~isostatic height and the density within

652 and beneath the lithosphere, would have a marginal contribution compared to

653 the mantle gravity residuals (Figure 11 (d), (e), (f) and Figure 12 (a), (b), (c))

654 which depend on the deeper density anomalies. ~~The observed~~ As this is what we

655 observe, we presume that the imbalance between the intensities of mantle

656 gravity residuals and the residual topography, which ~~is highlighted above all~~

657 ~~with~~we observe especially for the SII-ρ model, ~~reveals the plausible~~ is due to a

658 lateral viscosity ~~increase~~growth, associated with the increasing thickness and

659 density of the Pacific ~~plate~~Plate, from the ~~East Pacific Rise~~EPR towards west, up

660 to the Kermadec and Tonga Trench in the south and the Kuril-Kamchatka Trench

661 in the north~~.~~ (Figure 6 and Figure 15). However, although in the Northwestern

662 Pacific the surface uplift is presumably shallower than the mantle upwelling,

663 because it only compensates for a part of the mass deficit, ~~and the net residual~~

664 ~~topography is sensitive to the possible uncertainties in the density structure of~~

665 ~~the lithosphere, it still~~this occurrence does not explain the conjunction of

anomalous height of seafloor topography, the lack of a heat flow anomaly and the net geoid low observed in the ~~region~~regions around the Hawaiian Swell and South Pacific ~~Superswell (Fig. 10).~~ Super Swell (Figure 14).

Following McNutt (1998) and Mc Nutt and Bonneville (2000), who suggested that the discrepancy between the heat flow and depth of the lithosphere could imply that the origin of the ~~Superswell~~Super Swell is non-thermal (e.g. the convecting material beneath is low density by virtue of its mineralogy rather than its temperature), we ~~used our results to test this hypothesis. Optimizing the ρ-v_s correlation coefficient in 3 enabled us to obtain the 3-D map of lateral variations in the angular coefficients of the ρ-v_s coupling with respect to the 1-D thermal relationships, and to select the regions characterized by density compositional variations~~use our results on the optimization of the ρ-v_{SV} correlation coefficient (Fig. 7) to test this hypothesis. On the basis of our results ~~(Simmons et al., 2010, Tondi et al., 2012b). Figure 13 shows our interesting results. First of all compositional variations presumably only affect densities at the lithosphere asthenosphere boundary (LAB) as chemically induced density anomalies show up gradually from the Eastern to the North Western Pacific plate and do not extend below 200 km in depth. Thus~~, Mc Nutt's hypothesis is plausible, as chemically-induced density anomalies can be observed all along subducting slabs, beneath ~~the Superswell~~both the Hawaiian and the South Pacific Super Swell, and in the structure of the lithosphere between the Aleutian Trench and the Fiji North Plateau in the northwestern edge of the Plate. These observations are ~~partly~~also justified by the fact that perturbed phase relations among mantle minerals are expected within the thermal environment of subducting slabs (Bina et al., ~~2001). The important anomalies observed beneath~~

~~the northwestern part of the lithosphere, are unexpected, however they may help to explain some inconsistencies between geodetical and seismological observations. Infact, nearly all seismological studies (Forsyth, 1977, Zhang and Tanomoto, 1991, Maggi et al., 2006) show that lithospheric seismic velocities, the thickness of the seismic lithosphere and the seismic velocities in the low-velocity zone below the lithosphere all increase continuously with age when averaged over isochrons, and do not flatten out for older lithosphere in the same way that geoid and gravity observations do.~~

~~Thus, the non-thermal density anomalies at the base of the lithosphere may reduce the weight of the lithosphere in that part of the model and explain the modest impact on the gravity and geoid measurements.~~2001), In addition, the compositionally-induced density anomaly beneath the surface of both the ~~Superswell~~Swells, may explain why the measured average heat flow is not resolvably different from other Pacific values, ~~even though the~~ in spite of the presence of the topographic highs.

With regard to the geoid (Fig. 14), a semi continuous belt of lows surrounds the Pacific, including isolated minima in the Indian Ocean, Ross Sea and northeast Pacific. No corresponding negative anomalies are observed in the free-air and/or Bouguer gravity map and, as a consequence, no information is given by our study in this regard. As studied by Spasojevic et al., (2010), the geoid lows are correlated with high-velocity anomalies near the base of the mantle and low-velocity anomalies in the mid-to-upper mantle, hence they are not constrained by our density model.

A mass deficit up to depth of 150 km (Fig. 6), correlated with calculated positive residual topography (Fig. 11 g), h), i)) and observed positive geoid anomaly (Fig.

Formatted: Font color: Auto

Formatted: Font color: Auto

14) is instead reconstructed by our model beneath the Hawaiian chain. Following Cadio et al., (2012) the average depth of the ~~seafloor on the Superswell is consistently shallower.~~ compensating density anomaly, might indicate compensation within the asthenosphere such as by dynamic uplift, which is unfortunately not confirmed by our proxy of dynamic topography (Fig. 13). On the contrary, we are in favor of the presence of crustal underplating, that, as suggested by Leahy et al., (2010), and previously identified by the deep-penetrating marine refraction study of Watts et al., (1985) indicates that the Hawaiian Swell is partially supported by shallow chemical buoyancy which can be conveniently associated to the recovered compositional anomaly (Fig. 7). The geoid in the Super-Swell region, that following Adam and Bonneville (2004) covers an area between latitudes 10°N and 30°S and longitudes [130-160]°W, shows two different features: a positive anomaly in the northern branch, that becomes progressively negative towards the South. Correlated positive to negative density anomalies are reconstructed up to 100 km depth and below the lithosphere (Fig. 15). The analysis of the negative correlation between the residual topography and the mantle residual gravity evidences that in this region is active the contribution of mantle circulation in supporting the long-wavelength topography. This is particularly evident with the seismic model. With the SII model, the mantle support is of limited amplitude and more relevant in the northern part of the Swell (Fig. 13). As studied by Adam et al., (2014) dynamic topography is sensitive both to the viscosity profile and to the tomographic models. As suggested above, results support the presence of a lateral viscosity growth, associated with the increasing thickness of the Pacific plate. Hence we favor the presence of a low viscosity asthenosphere beneath the

Formatted: English (United Kingdom)

Formatted: Font color: Auto, English (United Kingdom)

South Pacific superswell, accordingly to the study of Adam et al., (2014). The presence of density compositional variations reduces the negative correlation between residual topography and the mantle residual gravity and this explains the differences of the results obtained with the seismic and the SII models. Density compositional variations, especially important in the Southern branch of the Swell, are also consistent with the hypothesized underplating beneath the Marquesas swell (McNutt and Bonneville, 2000). Surface topography of the Superswell region may then by explained by the joint contribution of dynamic topography and crustal underplating which offers another source for the buoyancy of the Swell and justifies the measured heat flow (Veselov and Lipina, 1982), which is not resolvably different from other Pacific values.

3. CONCLUSIONS

The exploitation of the information provided by the seismological and satellite gravity data, enabled us to contribute to the determination of ~~a high resolution density crustal~~ important physical and geological information within the lithospheric and upper mantle structure of the Pacific, down to ~~a~~ 300 km depth. ~~Our approach enabled us to recover a density earth structure which is~~ The recovered parameters on a uniform 1° x 1° grid , such as 1) the densities compatible with both seismological and gravity observations~~. In addition, a realistic relationship was obtained~~ and 2) the phase relationships between the isotropic shear-wave velocity and the density structure~~, from which~~ enabled us to extract useful and novel information on a) the thickness of the lithosphere, b) the thermally and chemically-induced density anomalies, ~~can then be extracted.~~c) the residual topography, d) the mantle gravity residuals, e) the

dynamic topography and f) midplate swells for the whole Pacific region. This information ~~could~~should help to reconcile some incompatible descriptions of the oceanic lithosphere of the Pacific ~~plate. .~~

Unlike the results of ~~the~~ tomographic inversion, ~~and in line with Dunn and Forsyth (2007),~~ the ~~positive~~negative density anomaly beneath the ~~East Pacific Rise is slightly visible~~ EPR are chemically induced at shallower depths, ~~becomes important between 200 and 250 km, and disappears at 300 km. With~~ thus confirming that the overall upwelling is passively driven by plate motions. Additionally, with respect to the seismological studies, we observe that ~~(~~1) the SII-ρ model shows a lighter lithosphere, ~~(2) positive flanked by negative chemically induced densities are located along the eastern boundary of the Pacific plate, (~~32) a wide area of strong positive ~~flanked~~densities strengthened by strong negative chemically-induced density anomalies is revealed between the Aleutian Trench and the Fiji Plateau in the northwestern edge of the Pacific plate, ~~(~~3) both the Hawaiian and the Super Swell are characterized by density compositional variations that may support the hypothesized crustal underplating, 4) the proxy of the contribution of mantle flow to the surface bathymetry is ~~limited mostly to the eastern side~~concentrated beside the western flank of the EPR and decreases progressively towards the western Pacific Plate, 5) the features of the recovered mantle gravity residuals evidence a lateral viscosity growth, associated with the increasing thickness of the Pacific Plate, from the EPR towards west, up to the Kermadec and Tonga Trench in the south and the Kuril-Kamchatka Trench in the north.

From these results, we conjecture that the cooled layer of mature lithosphere thickens with age as suggested by the dispersion of Rayleigh waves with oceanic

Formatted: Indent: First line: 1.25 cm

Formatted: Font color: Auto

paths (Zhang and Tanimoto, 1991. Maggi et al., 2006). However, from a depth of 70 to 150 km, pressures and temperatures chemically modify the composition of the lithospheric layer. This chemically-modified structure is lighter and more buoyant than the predicted cooling models, which reconciles gravity observations that do not show an increasing gradual negative gradient progressing towards the north-western side of the Plate. In addition, the existence of non-thermal sources of buoyancy at the base of the lithosphere, below the northwestern side and along the eastern boundary of the Pacific plate, also justifies the fact that the conducted heat flux stabilizes to a constant value of 50 to 60 ~~m W m^2~~ $\frac{W}{Km}$ after 25- or 30 million years (Stein, 1995) and does not vary significantly compared to other Pacific values, although the depth is different. Presumably, after this time, phase relations among mantle minerals start to be perturbed and the direct relationship between the convective material beneath and its temperature is progressively lost. Coherently with the observed chemically modified structures, results support also the hypothesis that midplate swells are not entirely explained by thermal and dynamic surface uplift from rising mantle plumes, but by a joint contribution of volcanic underplating and mantle flow.

~~Our proxy of the contribution of mantle flow to surface topography, is based on gravity residuals, which explains the lack of flow in the northwestern side of the SII-ρ model. As discussed above, the thickness of the lithosphere is consistent with the seismological observations, however due to density compositional variations, the lithosphere is lighter and as a consequence the convective flux beneath can reach the same result with a lower intensity.~~

Aknowledgments

The results in this paper were obtained thanks to the CINECA Italian SuperComputing Resource Allocation (ISCRA) HP10CNWW73 and HP10CJNYL3. A special thank of the authors to Dr. A. Maggi for supplying data and information related to the seismological model.

REFERENCES

Adam, C., Bonneville, A., 2004. Extent of the South Pacific Superswell, Journ. of Geophys. Res., 110, B09408, doi: 10.1029/2004JB003465

Adam C., Yoshida M., Suetsugu D., Fukao Y., Cadio C., 2014. Geodynamic modeling of the South Pacific superswell. PEPI, 229, 24-39, doi: 10.1016/j.pepi.2013.12.014

Afonso, J.C., Zlotnik, S., Fernandez, M., 2008. The effects of compositional and rheological stratifications on small-scale convection under the oceans: implications for the thickness of oceanic lithosphere and seafloor flattening. Geophys. Res. Lett. 35, L20308, doi:10.1029/2008GL035419.

Amante, C. ~~and B.W.~~, Eakins, B.W., 2009. ETOPO1 1 Arc-Minute Global Relief Model: Procedures, Data Sources and Analysis. NOAA Technical Memorandum NESDIS NGDC-24. National Geophysical Data Center, NOAA.

Formatted: English (United States)

Formatted: English (United States)

Formatted: English (United States)

Formatted: English (United States)

Formatted: English (United States)

Formatted: English (United States)

doi:10.7289/V5C8276M

Bina, C. R., Stein, S., Marton, F. C., Van Ark, E. M., 2001. Implication of slab mineralogy for subduction dynamics, Physics of the Earth and Planetary Interiors, 127, 51-66.

Birch, F. (., 1964). Density and composition of mantle and core, J. Geophys. Res., 69(20), 4377–4384.

Blakely, R. J. (., 1995). Potential Theory in Gravity and Magnetic Applications, Cambridge Univ. Press, New York.

Boschi, L., Faccenna, C., and Becker, T.W., 2010. Mantle structure and dynamic topography in the Mediterranean Basin. Geophys. Res. Lett., 37, L20303, doi.10.1029/2010GL045001.

Cadio, C., Ballmer, M.D., Panet, I., Diament, M., Ribe, N., 2012. Constraints on the origin of the Hawaiian swell from wavelet analysis of the geoid to topography ratio, EPSL, 359-360, 40-54.

Cammarano, F., A. Deuss, S.A., Goes, and D.S., Giardini (, D., 2005), One dimensional physical reference models for the upper-mantle and transition zone: Combining seismic and mineral physics constraints, J. Geophys. Res., 110, B01306, doi:10.1029/2004JB003272.

Formatted: Font: Not Italic, Italian (Italy)
Formatted: Font: Not Italic, Italian (Italy)
Formatted: Font: Not Italic, Italian (Italy)
Formatted: Font: Not Italic, Italian (Italy)
Formatted: Font: Not Italic, Italian (Italy)
Formatted: Font: Not Italic, Italian (Italy)
Formatted: Font: Not Italic, Italian (Italy)
Formatted: Font: Not Italic, Italian (Italy)
Formatted: Font: Not Italic, Italian (Italy)
Formatted: Font: Not Italic, Italian (Italy)
Formatted: Font: Not Italic, Italian (Italy)
Formatted: Font: Not Italic, Italian (Italy)
Formatted: Italian (Italy)

Caratori Tontini, F., Graziano, F., Cocchi, L., Carmisciano, C., ~~and~~ Stefanelli, P., 2007. Determining the optimal Bouguer density for a gravity data set: Implications for the isostatic setting of the Mediterranean Sea. Geophys. J. Int., 169, 380–388.

Chung, D.~~-~~H. ~~(~~, 1972~~),~~ Birch's law: Why is it so good?, Science, 177, 261–263.

Dávila, F., Lithgow-Bertelloni, C., 2013. Dynamic topography in South America. Journal of South American Earth Sciences, 43, 127-144.

Drinkwater, M.R., Floberghagen, R., Haagmans, R., Muzi, D. and Popescu, A., 2003. GOCE: ESA's first Explorer Core mission. Space Science Reviews, 108, 419-432.

Dunn, R.A., ~~and~~ Forsyth, D.W., 2007. Crust and lithospheric structure – Seismic structure of Mid-Ocean Ridges. In Treatise of Geophysics, Elsevier, ~~-~~ISBN: 978-0-444-52748-6, pp 419-443.

Doin, M.P., Fleitout, L., 2000. Flattening of the oceanic topography and geoid: Thermal versus dynamic origin. Geophysical Journal International, 143, 582-594.

Dziewonski, A.~~-~~M., ~~and D. L.~~ Anderson ~~(~~, D.L., 1981~~),~~ Preliminary reference Earth model, Phys. Earth Planet. Inter., 25, 297–356.

Ekstrom, G., ~~and~~ Dziewonski, A.~~-~~M., ~~(~~1998~~),~~ The unique anisotropy of the Pacific upper mantle, Nature, 394, 168-172.

Formatted: Font: Not Italic, Italian (Italy)

Formatted: Font: Not Italic, Italian (Italy)

Formatted: Font: Not Italic, English (United States)

Formatted: Font: Not Italic, English (United States)

Formatted: Justified

Formatted: Font: Not Italic, English (United States)

Formatted: Font: Not Italic, English (United States)

Formatted: English (United States)

Formatted: Font: +Body, English (United States)

Forsyth, D., 1977. The evolution of the upper mantle beneath mid-ocean ridges, Tectonophysics, 38, 89–118.

Forte, A.M., 2007. Constraints on seismic models from other disciplines — implications for mantle dynamics and composition. In: Romanowicz, B., Dziewonski, A.M. (Eds.), Volume 1 of Treatise of Geophysics. Elsevier, pp. 805–858.

Flament, N., Gurnis, M., and Müller, R. D., 2013. A review of observations and models of dynamic topography. Lithosphere, 5, (2), 189-210.

Gilardoni, M., Reguzzoni, M., Sampietro, D. and Sansò, F., 2013. Combining EGM2008 with GOCE gravity models. Bollettino di Geofisica Teorica e Applicata, 54 (4), 285-302.

Heiskanen, W.A. and Moritz, H., 1967. Physical Geodesy. Freeman, San Francisco.

Jarvis, G.T., Peltier, W.R., 1982. Mantle convection as a boundary layer phenomenon. Geophysical Journal of the Royal Astronomical Society, 68, 385-424.

Kido, M., Seno, T., 1994. Dynamic topography compared with residual depth

Formatted: Italian (Italy)

Formatted: Italian (Italy)

anomalies in oceans and implications for age-depth curves. Geoph. Res. Lett., 21, 717-720.

Kozlovskaya, E., T. Janik, J.T., Yliniemi, G.J., Karateyev, and M.G., Grad (, M., 2004),. Density-velocity relationship in the upper lithosphere obtained from P- and S-wave velocity models along the Eurobridge'97 seismic profile and gravity data, Acta Geophys. Pol., 52(4), 397–424.

Leahy, G.M., Collins, J.A., Wolfe, C.J., Laske, G., Solomon, S.C., 2010. Underplating of the Hawaiian Swell: evidence from teleseismic receiver functions, Geoph. J. Int., 183, 313-329.

Maggi, A., Debayle, E., Priestley, K., and Barruol, G., 2006. Multimode surface waveform tomography of the Pacific Ocean: a closer look at the lithospheric cooling signature. Geophys. J. Int., 166, 1384–1397, doi: 10.1111/j.1365-246X.2006.03037.x.

Mayer-Gürr, T., 2006. Gravitationsfeldbestimmung aus der Analyse kurzer Bahngen am Beispiel der Satellitenmissionen CHAMP und GRACE (PhD thesis). University of Bonn, Germany.

McKenzie, D.–P., 1967. Some remarks on heat flow and gravity anomalies, J. Geophys. Res., 72(6), 261–266, 273.

Mc Nutt, M. McNutt, M.K, Bonneville, A., 2000. A shallow, chemical origin for the

Formatted: English (United States)
Formatted: English (United States)
Formatted: English (United States)
Formatted: English (United States)
Formatted: English (United States)
Formatted: English (United States)
Formatted: English (United States)
Formatted: Italian (Italy)
Formatted: Italian (Italy)
Formatted: Italian (Italy)

Marquesas swell. Geochemistry Geophysics Geosystems, Vol. 1, 6, DOI: 10.1029/1999GC000028

McNutt, M.K., 1998. Superswells. Reviews of Geophysics, 36 (2), 211-244.

Müller, R.D., Sdrolias, M., Gaina, C. and., Roest, W.R., 2008. Age spreading rates and spreading asymmetry of the world's ocean crust. Geochemistry, Geophysics, Geosystems, 9, Q04006, doi:10.1029/2007GC001743.

Nataf, H.-C., and Y. Ricard (, Y., 1996),. 3SMAC: an a priori tomographic model of the upper mantle based on geophysical modelling, Phys. Earth Planet. Inter., 95, 101– 122, doi:10.1016/0031-9201(95)03105-7.

Pail, R., Bruinsma, S., Migliaccio, F., Förste, C., Goiginger, H., Schuh, W.D., Höck, E., Reguzzoni, M., Brockmann, J.M., Abrikosov, O., Veicherts, M., Fecher, T., Mayerhofer, R., Kransbutter, I., Sansò, F. and., Tscherning, C.C., 2011. First GOCE gravity field models derived by three different approaches. J. Geod., 85(11), 819-843.

Panasyuk, S. V., and B. H. Hager, B.H., 2000. Models of isostatic and dynamic topography, geoid anomalies, and their uncertainties, J. Geophys. Res., 105, B12, 28, 199–28,209.

Pavlis, N.A., Holmes, S.A., Kenyon, S.C. and., Factor, J.K., 2012. The development

Formatted: English (United States)

Formatted: English (United States)

Formatted: English (United States)

and evaluation of the Earth Gravitational Model 2008 (EGM2008). J. Geophys. Res., 117, B4.

Parker, R. & Oldenburg, D., 1973. Thermal model of ocean ridges, Nature, 242, 137–139.

Pekeris, C. L., 1935. Thermal convection in the interior of the Earth, Geophys. J. Int., 3, 343–367, doi:10.1111/j.1365-246X.1935.tb01742.x.

Richards, M. A., and Hager, B. H., 1984. Geoid anomalies in a dynamic Earth, J. Geophys. Res., 89, 5987–6002.

Simmons, N. A., A. M. Forte, L. Boschi, and S. Grand (2010),Simmons, N.A., Forte, A.M., Grand, S.P., 2009. Joint seismic, geodynamic and mineral physical constraints on three-dimensional mantle heterogeneity: Implications for the relative importance of thermal versus compositional heterogeneity, Geophys. J. Int., 177, 1284-1304.

Simmons, N.A., Forte, A.M., Boschi, L., Grand, S., 2010. GyPSuM: A joint tomographic model of mantle density and seismic wave speeds, J. Geophys. Res., 115, B12310, doi:10.1029/2010JB007631.

Smith, W.H.F., Sandwell, D.T., 1997. Global sea floor topography from satellite altimetry and ship depth soundings. Science, 277, 1956-1962.

Stein, C.A., 1995. Heat flow from the Earth. In Ahrens T.J., Global Earth Physics, A Handbook of Physical Constants, Washington, AGU.

Schubert, G., Turcotte, D.L., Olson, P., 2001. Mantle Convection in the Earth and Planets, Cambridge University Press, Cambridge.

Spasojevic, S., Gurnis, M., Sutherland, R., 2010. Mantle upwellings above slab graveyards linked to the global geoid lows, Nature Geoscience, 3, 435-438.

Stein, C.A., and Stein, S., 1992. A model for the global variation in oceanic depth and heat flow with lithospheric age. Nature 359, 123.

Tondi, R., de Franco, R., and Barzaghi, R., 2000. Sequential integrated inversion of refraction and wide-angle reflection traveltimes and gravity data for two-dimensional velocity structures. Geophys. J. Int., 141, 679-698, doi: 10.1046/j.1365-246x.2000.00104.x

Tondi, R., Cavazzoni, C., and Morelli, A., 2012a. Parallel "large" dense matrix problems: Application to 3D joint inversion of seismological and gravity data. Comput. Geosci., 48, 143-156, doi:10.1016/j.cageo.2012.05.026.

Tondi, R., de Franco, R., 2006. Accurate assessment of 3D crustal velocity and density parameters: Application to Vesuvius data sets. Phys. of the Earth and Plan. Int., 159, 183-201.

Formatted: Italian (Italy)
Formatted: Italian (Italy)
Formatted: Italian (Italy)
Formatted: Italian (Italy)
Formatted: Italian (Italy)
Formatted: Italian (Italy)
Formatted: Italian (Italy)
Formatted: Italian (Italy)
Formatted: Italian (Italy)

Tondi, R., Schivardi, R., Molinari, I., Morelli, A., 2012b. Upper mantle structure below the European continent: Constraints from surface-wave tomography and GRACE satellite gravity data. J. geophys. Res., 117, B09401, doi:10.1029/2012JB009149.

Veselov, O.V., and Lipina, E.N., 1982. Catalogue of heat flow data from East of Asia, Australia and West Pacific Ocean, World Data Center for Solid Earth Physics.

Watts, A.B., Ten Brink U.S., Buhl P, and Brocher T.M., 1985. A Multichannel seismic study of lithospheric flexure across the Hawaiian-Emperor seamount chain, Nature 315, 105-111.

Zhang, Y.S. ~~and.,~~ Tanimoto, T., 1991. Global Love wave phase velocity variation and its significance to plate tectonics. Phys. Earth Planet. Inter., 66, 160-202.

Zhang, N., Zhong, S., Flowers, R.M., 2012. Predicting and testing continental vertical motion histories since the Paleozoic. Earth and Planetary Science Letters, 317–318, 426–435, doi:10.1016/j.epsl.2011.10.041.

Zhao, D., Mishra, O. ~~&.,~~ Sanda, R., 2002. Influence of fluids and magma on earthquakes: seismological evidence. Phys. Earth planet. Inter., 132, 249–267.

Formatted: Italian (Italy)

Formatted: Italian (Italy)

Figure captions

Fig. 1. Latitude-dependent standard deviation of the GOCE-only model commission error [mgal].

Fig. ~~2. Flow chart of the inversion procedure, including optimization of density and velocity~~2: (a) Free-air gravity anomalies from 128,880 points of the combined GOCE-EGM2008 model over the study area (degree 2190). b) Bouguer anomaly map of the Pacific Plate recovered from (a). See paragraph 2.1 for details.

Fig. 3~~:~~. Flow chart of the inversion procedure, including optimization of density and velocity.

Fig. 4. Comparison among (a) ~~128,880 free-air~~the mean diagonal elements of the *a posteriori* seismic standard deviation, (b) the assigned mean diagonal elements of the C_{mm} covariance matrix (takes in account the error propagation from the velocity model to the density model and (c) the mean density update of the first iteration ($\Delta\rho^1$)

Fig. 5. Sketch of the followed steps to recover (d) the diagonal values of the correlation matrix between the residual topography and the mantle residual gravity anomalies ~~from~~produced by the ~~combined GOCE-EGM2008~~SII density model ~~over~~. As an example, (a) a vertical slice through the ~~study area (degree 2190). Minimum value~~recovered model (30° N) is ~~-340,29 mgal, maximum~~

Formatted: Widow/Orphan control, Adjust space between Latin and Asian text, Adjust space between Asian text and numbers

~~value~~analyzed. The method used to determine the depth of the lithosphere is ~~523,80 mgal. (b) Bouguer~~explained in the text. Following Pekeris (1935) and Hager et al., (1985), (d) the negative correlation between (b) the mantle residual gravity anomaly ~~map of the Pacific Plate recovered from (a).~~and (c) the residual topography, may identify the regions where the contribution of mantle circulation in supporting the long-wavelength topography is active.

Fig. ~~4.~~6. Depth sections of the ρ percentage perturbations in (a) our optimized SII-ρ model ~~(a).~~ Model perturbations are expressed as percentage deviations with respect to (b) the mean density value of each layer ~~plotted in (b).~~ In ~~the first~~ [redacted] ~~(~~each section~~),~~ the main tectonic units are indicated. In (b) the depth interval of the lithosphere in 1-D SII-ρ, PREM and seismic model (Maggi et al., 2006) are shown. The area of the Pacific Superswell, identified by Adam and Bonneville (2005), is superimposed on each section.

Formatted: Widow/Orphan control, Adjust space between Latin and Asian text, Adjust space between Asian text and numbers

Fig.

~~Figure 5~~7. Depth sections of the lateral differences in the optimized angular coefficient α with respect to the a priori Birch coefficients (0.72 for 50 km depth, 0.34 from 100 to 200 km depth). The area of the Pacific Superswell, identified by Adam and Bonneville (2005), is superimposed on each section.

Fig. 8. Bouguer anomaly map reproduced by SII-ρ model in Fig. ~~4~~6 (a). Gravity misfit with respect to observations in Fig. ~~3~~2 (b) is 66.73 ~~mgals~~mgal and variance reduction is 67.4%.

Fig. 9. Density values from the recovered SII-ρ model in Fig. 6(a), plotted against the velocity values from the seismological model and compared to Birch law regression lines (black solid lines), our $v_{SVm}^0 - \rho_m^0$ starting relationship .

Fig. 10.

~~Fig. 6.~~ Depth sections of *a-posteriori* percentage standard deviation on SII-ρ model. Standard deviation takes into account the propagation of uncertainty from the velocity to the density model, weighted with the final gravity variance reduction Var(~~gi),g(n)),~~ and the information given by the gravity data~~. Images relative~~ (eq. (8)). In each section, the standard deviation values are referred to the ~~mean of the 3~~1-D SII-ρ model, imaged in Fig. ~~4~~6 (b~~) at each depth indicated.~~). In the first ~~(~~section~~),~~ the main ~~tectonical~~tectonic units are indicated.

Fig. ~~7~~11. (a), (b) (c) Calculated lithospheric thickness of the Pacific region, derived mostly from Müller et al., (~~1997~~2008) isochrones (see text for additional information). (b) shows the mean value and (a) and (c) show the mean value minus and plus the standard deviation respectively. (d),(e),(f) Mantle residual gravity anomalies (background density is adjusted in order to magnify the contrast between ocean and continents) calculated assuming the SII density model and the lithospheric depth in (a), (b) and (c). ~~(g), (h), (i) Residual topography of the Pacific region, calculated assuming the SII-r density model and the lithospheric depth in (a), (b) and (c).~~ (g), (h), (i) Residual topography of the Pacific region, calculated assuming the SII-ρ density model and the lithospheric depth in (a), (b) and (c).

Formatted: English (United States)

Formatted: English (United States)

Formatted: English (United States)

Formatted: English (United States)

Formatted: English (United States)

The area of the Pacific Superswell, identified by Adam and Bonneville (2005), is superimposed on each section.

Fig. ~~8~~12. (a), (b) (c) Mantle residual gravity anomalies calculated assuming that the seismic model has been transformed into a density model ~~–~~through the starting ρ-vSV depth-dependent relationship and the lithospheric depth in Fig. ~~7~~11 (a), (b) and (c).

(d), (e), (f) Residual topography of the Pacific region, calculated assuming the seismic model transformed in a density model through the starting ρ-vSV depth-dependent relationship ~~-~~and the lithospheric depth in Fig. ~~7~~11 (a), (b) and (c).

The area of the Pacific Superswell, identified by Adam and Bonneville (2005), is superimposed on each section.

Fig. ~~9:~~13. (a), (b), (c) Proxy of dynamic topography ~~assuming~~for the seismic model transformed in a density model through the starting ρ-vSV depth-dependent ~~relationship (Birch) and the lithospheric depth in Fig. 7 (a), (b) and (c).~~ .

(d), (e), (f) Proxy of dynamic topography for the SII-ρ model. Contour plots highlight the areas of negative relationship between the residual topography (subtracted by mean + standard deviation) and the mantle residual gravity (subtracted by mean + standard deviation) of the Pacific region. ~~-~~The area of the Pacific Superswell, identified by Adam and Bonneville (2005), is superimposed on each section.

Formatted: English (United States)
Formatted: English (United States)
Formatted: English (United States)
Formatted: English (United States)
Formatted: English (United States)
Formatted: English (United States)
Formatted: English (United States)
Formatted: English (United States)
Formatted: English (United States)
Formatted: Widow/Orphan control, Adjust space between Latin and Asian text, Adjust space between Asian text and numbers
Formatted: English (United States)
Formatted: English (United States)
Formatted: English (United States)
Formatted: English (United States)
Formatted: English (United States)
Formatted: English (United States)

Fig. ~~10~~14. Geoid ~~anomalies~~undulations from the combined GOCE-EGM2008 model over the study area. Minimum value is -68,~~472~~847 m, maximum value is 87,~~362~~336 m. The area of the Pacific Superswell, identified by Adam and Bonneville (2005), is superimposed. The main tectonic units are indicated.

~~Fig. 11. Density values from the recovered SH-ρ model in Fig. 4(a), plotted against the velocity values from the seismological model and compared to Birch law regression lines (black solid lines).~~

~~Fig. 12. Isosurface~~15. Isosurfaces of densities characterizing the ~~cool (3520 kg/m3) and the warm (3470 kg/m3)~~ structures of the upper mantle below the Pacific region as seen (a) directly overhead and in a ~~(a) vertical and~~3-D view (b) ~~horizontal 3D visualization of SH-ρ model.~~ cut from 50 km depth, (c) cut from 150 km depth, (d) cut from 250 km depth. Earthquakes from ISC and NEIC catalogues are shown as blue ~~triangles~~stars for magnitudes between 7.0 and 7.5~~,~~ and as black circles and as ~~magenta~~black circles for magnitude greater than 7.5. ~~The coastlines are shown in black, and the Superswell area is inside the yellow rectangle (Adam and Bonneville, 2005).~~

~~Fig. 13. Depth sections~~The area of the ~~lateral differences in the optimized angular coefficient α with respect to the a priori Birch coefficients (.72 for 50 km depth, .34 from 100 to 200 km depth and .53 from 250 to 300 km depth. The location of the~~Pacific Superswell, identified by Adam and Bonneville (2005), is ~~indicated in the first section by two horizontal lines.~~superimposed on each plot.

Formatted: English (United States)

1157

The combined inversion of seismological and GOCE gravity data: New insights into the current state of the Pacific lithosphere and upper mantle

Rosaria Tondi[1], Maddalena Gilardoni[2], Mirko Reguzzoni[2]

[1]*Istituto Nazionale di Geofisica e Vulcanologia, Via Donato Creti 12, 40128 Bologna, sezione di Bologna, Italy*

[2]*DICA, Politecnico di Milano, P.zza Leonardo da Vinci 32, 20133 Milano, Italy*

ABSTRACT

In this study we combine seismological and GOCE satellite gravity information by using a Bayesian-like technique, with the aim of inferring the density structure of the Pacific (90°N 90°S) (121°E 60°W) lithosphere and upper mantle.

We recover a 1° x 1° 3-D density model, down to 300 km depth, which explains gravity observations with a variance reduction of 67.41%. The model, with an associated *a posteriori* standard deviation, provides a significant contribution to understanding the evolution of the Pacific lithosphere and answer to some debated geodynamic questions.

Our methodology enables us to combine the recovery of density parameters with the optimum density-v_{SV} scalings. The latter account for both seismological and gravity observations in order to identify the regions characterized by chemically-induced density heterogeneities which add to the thermally-induced anomalies. Chemically-modified structures are found west of the East Pacific Rise (EPR) and are of relevant amplitude both below the north-western side of the Pacific Plate, at the base of the lithosphere, and up to 100 km depth beneath the Hawaiian and Super Swell regions, thus explaining the anomalous shallow regions without

invoking as the sole justification the thermal buoyancy. Coherently with the chemically modified structures, our results a) support a lighter and more buoyant lithosphere than that predicted by the cooling models and b) are in favor of the hypothesized crustal underplating beneath the Hawaiian chain and beneath the volcanic units in the southern branch of the Super Swell region. The comparison between calculated mantle gravity residuals and residual topography suggests a) a lateral viscosity growth associated with the increasing thickness and density of the Plate and b) correlate well with sub-lithospheric mantle flow from the EPR towards west, up to the Kermadec and Tonga Trench in the south and the Kuril-Kamchatka Trench in the north.

1. INTRODUCTION

The topography of the Earth's surface is explained by the combined effects of shallow processes such as erosion or sedimentation, and deeper ones such as isostatic compensation and the upward push/downward pull associated with a convective flow in the mantle (Richards and Hager, 1984). The latter effect, known as dynamic topography, has been evaluated in a number of studies, where models of mantle density are defined on the basis of seismic tomography, and used to predict the associated mantle flow (Forte, 2007, Boschi et al., 2010, Dávila and Lithgow-Bertelloni, 2013, Flament et al., 2013). Yet, given the number of dynamic processes that affect the topography, researchers still haven't reached a consensus about the term "dynamic topography" and the absence of a detailed knowledge of the thermal and chemical structure of the lithosphere, effectively limits the possibility to discriminate among a number of different solutions. As an example, the bathymetry of the young ocean floor (<80 Ma) is compatible with

51 that of the thermal boundary layer of the convecting mantle, and, in this respect, the
52 subsidence of oceanic lithosphere with age should be included in the definition of
53 dynamic topography. On the other side, ocean floor older than ca. 80 Ma appears to
54 flatten compared to the two main boundary-layer cooling models (McKenzie,
55 1967, Stein and Stein, 1992, Parker and Oldenburg, 1973), which have been
56 produced to explain the observed variation of heat flow and oceanic depth with
57 age. Additionally, due to its long and complex tectonic history, the dynamics of the
58 continental lithosphere cannot be explained by a boundary layer theory.

59 Goal of this paper is to obtain means for constraining convective circulation of
60 the sub-lithospheric mantle of the Pacific Plate through the analysis of the physical
61 parameters of the oceanic lithosphere. The Pacific region is a natural laboratory for
62 oceanic plate tectonics and it contains not only relatively large areas of old
63 seafloor, but also numerous hot spot tracks, that may have a role in transporting
64 heat to the bottom of the thermal boundary layer. As recalled above, numerous
65 studies have found that seafloor older than 80 Ma reaches depths several
66 hundred meters shallower than would be predicted by the two main lithospheric
67 cooling models (McKenzie, 1967, Stein and Stein, 1992, Parker and Oldenburg,
68 1973) and no general consensus has yet emerged on a single mechanism of
69 heating that can explain all available observations. Several recent studies have
70 continued to refine these early interpretations of a seafloor depth-age
71 relationship. Proposed explanations include constant heat flux from below (Doin and
72 Fleitout, 1996), thermal rejuvenation by hotspots (Smith and Sandwell, 1997), small-
73 scale convection (e.g., Afonso et al., 2008), dynamic support by mantle flow (Kido
74 and Seno, 1994; Zhang et al., 2012), and departure from the topography predicted by
75 thermal boundary layer theory due to radioactive heat production within the mantle

(Jarvis and Peltier, 1982).

In any case, the sophistication and complexity of numerical approaches to determine the role of mantle-lithosphere interactions in shaping surface topography, cannot exempt researchers from studying and reconstructing the fine-scale structure of the lithosphere.

Seismically derived models of lithosphere suffer from incomplete ray coverage or limited data resolution, especially above oceans, where seismic stations, almost exclusively land based, are concentrated at the borders of the seafloor. For example, on the basis of the surface wave tomography of the Pacific mantle, Ritzwoller et al. (2004) have suggested that old lithosphere does not follow half-space cooling, however the spatial resolution of their tomography does not enable them to rule out that there may be a flattening effect of hotspot chains and oceanic plateaus.

On the other hand, surface observables such as gravity fields and geoid, which are directly dependent on the structure of the underlying distribution of mass, and recently benefit from the information released by space gravity missions such as GRACE and GOCE, are far superior in terms of spatial resolution, but still have to overcome the inherent non-uniqueness of any potential field method (Blakely, 1995). Additionally, in gravity analyses, errors can occur if internal boundaries (chemical or phase) with density contrasts, or the Earth's viscosity structure are not appropriately considered: if a low viscosity zone lies between an upwelling mass and the Earth's surface, the rising mass will then be relatively inefficient at warping the surface and will be largely compensated for from below, through the deformation of deeper density discontinuities (Mc Nutt, 1998).

An attempt to integrate seismological and gravity observations in the Pacific area is given by the global model of Simmons et al. (2010), which simultaneously considered seismic observations and a large suite of convection-related geodynamic constraints to obtain a three-dimensional (3-D) model of mantle density, shear wave speeds, and compressional-wave speeds. The results enabled Simmons et al. (2010) to simultaneously reconcile dynamic topography and gravity, to a wide extent (72%). They succeeded in distinguishing the thermal from the compositional contribution to both seismic velocities and densities. However, the resolution of the model is still not sufficient for continental studies (approximately 2.5° x 2.5° x 75 to 240 layer thickness). In terms of the Pacific Plate, the model does not discriminate the boundary layer between the lithosphere and the asthenosphere, which could help to resolve what happens to lithosphere plates older than 80 Ma.

In this paper we test the possibility of using integrated approaches, which consider both seismic and gravity constraints, in order to recover a high-resolution 3-D density model of the upper mantle and the lithosphere of the Pacific Region, with a lateral resolution of 1° x 1°, down to a 300 km depth and use it as a proxy for dynamic topography. Density anomalies are recovered using the inversion approach of Sequential Integrated Inversion (SII; (Tondi et al., 2000)), which has been parallelized to allow for a large data set and a large number of parameters (Tondi et al., 2012). We specify an initial mean 1-D density model within a volume of 179° x 177° x 300 km that is updated to a 3-D density model (179 x 177 x 17 model parameters) through the combined use of the surface waveform tomography of the Pacific upper mantle (Maggi et al., 2006) and a gravity model from the ESA Earth's explorer GOCE (Gravity field and

Ocean Circulation Explorer) mission (Drinkwater et al., 2003). Assuming that the Earth's lithosphere is the upper cold thermal boundary layer of a convecting system, the thickness of the lithosphere in our model is determined with Müller et al., (2008) isochrons and, where this information is not available, or is in contrast with the above physical assumption, we assign the depth where we observe a decrease in the depth-density curve of our final 3-D density model (hereinafter referred to as SII-ρ). The gravity field calculated for the SII-ρ structure, limited to the depth of the lithosphere, enables us to recover both the residual topography and the mantle residual gravity anomalies. Finally, we show that an estimation of the correlation matrix between the residual topography and the mantle residual gravity anomalies gives a proxy of the regions where the convective circulation of the sublithospheric mantle contributes to surface topography. In order to observe the added value of our approach, results obtained with the SII-ρ structure and those recovered from the density model, directly converted from seismic data are compared. The *a posteriori* standard deviation associated with the updated density parameters enables the reader to quantify the reliability of the results. Additionally, a fully 3-D map of the ρ-v_{SV} scaling relationships will help to better understand and interpret the interplay among the geodynamic features and processes that occur beneath and on top of the Pacific Plate.

2. DATA AND METHODS

2.1. The gravity database

The GOCE mission provides independent estimates of the Earth's

gravitational field, thus improving the present knowledge of low and medium frequencies and reducing systematic effects (bias and trend) at a local scale. To obtain free-air gravity anomalies from the GOCE mission data, we used the fourth release of the time-wise spherical harmonic expansion (Pail et al. 2011). This is a GOCE-only solution (no GRACE data are included) complete up to degree and order 250. The global commission error at this maximum degree is 3.93 mgal (Figure 1), while the omission error computed from EGM2008 degree variances (Pavlis et al. 2012) is 13.77 mgal. Consequently, the GOCE-only solution is combined with the EGM2008 ultra-high resolution global gravitational model, which is also based on ground and altimetry data, as well as a GRACE model (Mayer-Gürr 2006). Details on the combination weighting strategy, which is only driven by the coefficient error variances, are given in Gilardoni et al., (2013). Using this model the commission error up to the maximum degree of 2190 is about 4.01 mgal, as the omission error is practically negligible. Once the spherical harmonic coefficients have been chosen and the contributions of the normal potential have been removed (Heiskanen and Moritz 1967), free-air gravity anomalies in spherical approximation are computed by a classical synthesis operation, i.e.

$$\Delta g(\varphi,\lambda,r)=\frac{GM}{R^2}\sum_{n=2}^{N}\left(\frac{R}{r}\right)^{n+2}(n-1)\sum_{m=-n}^{n}T_{nm}Y_{nm}(\varphi,\lambda) \qquad (1)$$

where (φ, λ, r) are the spherical coordinates of grid points over the reference ellipsoid, GM is the gravitational constant by the Earth's mass, R is a reference Earth radius, Y_{nm} are the spherical harmonics of degree n and order m, and T_{nm} are the coefficients of the series truncated at the maximum degree N. A map of the computed gravity anomalies from the combined GOCE-EGM2008 model is

shown in Figure 2(a).

The availability of a topography/bathymetry dataset in resolutions up to 1 arc minute (ETOPO1, Amante and Eakins, 2009) enables us to calculate the Bouguer gravity map with a Bouguer density correction of 2670 kg/m^3 on land and a correction of -1640 kg/m^3 to correct for bathymetry (Caratori Tontini et al. (2007)). The Bouguer gravity anomalies, shown in Figure 2(b) are used as gravity observations for the optimization of the density parameters. On the basis of the estimated commission error, the a-priori gravity data error is set at 4.0 mgal for all the measurements (the square root of the diagonal elements of $\mathbf{C}_{gg}$).

2.2. Design of a 3-D density model

The Sequential Integrated Inversion (SII, Tondi et al., 2012) involves finding the maximum of a likelihood function (L) that relates density Earth structure (ρ) to our gravity observations ($\mathbf{g}$) and our seismic velocity structure ($\mathbf{v}$) through three types of information: (i) gravity data, (ii) information from the analysis of a seismological data-set ($\Delta\boldsymbol{v}$), and the (iii) information on the physical correlation between the density and the velocity parameters (α, C_{mm}):

$$L(\Delta\boldsymbol{g},\ \Delta\rho, \Delta\boldsymbol{v}) = exp\left\{-\frac{1}{2}[\Delta\boldsymbol{g} - G\,\Delta\rho]^T C_{gg}^{-1}[\Delta\boldsymbol{g} - G\,\Delta\rho]\right\}$$

$$x\ exp\left\{-\tfrac{1}{2}[\Delta\rho - \alpha\,\Delta\boldsymbol{v}]^T C_{mm}^{-1}[\Delta\rho - \alpha\,\Delta\boldsymbol{v}]\right\} \qquad (2)$$

The resulting SII algorithm allows the iterative estimation of the update ($\Delta\rho$) to the starting density model (ρ_0):

$$\Delta\boldsymbol{\rho} = (\mathbf{G}^{\mathrm{T}}\mathbf{C}_{\mathrm{gg}}^{-1}\mathbf{G} + \mathbf{C}_{\mathrm{mm}}^{-1})^{-1}\,(\mathbf{G}^{\mathrm{T}}\mathbf{C}_{\mathrm{gg}}^{-1}\Delta\mathbf{g} + \alpha\mathbf{C}_{\mathrm{mm}}^{-1}\Delta\mathbf{v}) \qquad (3)$$

where $\mathbf{G}$ is the matrix of the partial derivatives of the gravity observations ($\mathbf{g}$ = [g_1, g_2, …g_N], n ∈ [1,N]) with respect to the density model parameters ($\rho^{(i)}$ = [ρ_1,

198 ρ_2, … ρ_M], m∈ [1,M]), $\mathbf{C}_{gg}$ is the square diagonal covariance matrix of the gravity
199 data uncertainties, $\mathbf{C}_{mm}$ is the covariance matrix that takes into account the error
200 propagation from the velocity to the density model, $\Delta\mathbf{g} = (\mathbf{g}^{OBS} - \mathbf{g}^{i})$ the i-th model
201 predicted gravity response, $\alpha = [\alpha_1, \alpha_2, \ldots\alpha_M]$, m∈ [1,M] the velocity-density
202 gradient vector, in the same parametrization as the model, $\Delta\mathbf{v} = (\boldsymbol{v} - \boldsymbol{v}^0)$, the
203 velocity parameter adjustment vector of dimension M.
204 The flow chart in Figure 3 schematically summarizes the processing steps of the
205 inversion procedure. According to Maggi et al., (2006), our starting velocity
206 model ($\boldsymbol{v}^0$) is the superposition of the average crustal part of the 3SMAC (Nataf
207 and Ricard, 1996) 3-D Earth model and the smoothed version of the 1-D $\boldsymbol{v}_{SV}$
208 profile from PREM (Dziewonski and Anderson, 1981). The model covers the
209 whole Oceanic plate (90°N 90°S) (121°E 60°W) up to a depth of 400 km and is
210 parametrized with a rectangular grid with a spatial resolution of 1° x 1° x 17
211 layers of variable depth.
212 The seismic update ($\Delta\boldsymbol{v}_{SV}^{\mathbf{0}}$) is recovered from the regional surface waveform
213 tomography of the Pacific upper mantle, obtained using an automated
214 multimode surface waveform inversion technique on fundamental and higher
215 mode Rayleigh waves (Maggi et al., 2006). Considering the proved relationships
216 between the isotropic shear-wave velocity and the density parameters
217 [Kozlovskaia et al., 2004), only the isotropic shear-wave speeds have been
218 considered.
219 With regard to the starting density model ($\boldsymbol{\rho}^0$), it is obtained from the starting
220 velocity model ($\boldsymbol{v}^0$) through an *a priori* v_{SV}-ρ depth-dependent relationship. In
221 order to ensure the optimum choice of physical relationships between the

seismic velocities and bulk densities:

1. We assume a node-dependent linear relationship: $\rho_m = \alpha_m v_m + \beta_m$, i.e. with a-priori information we can use different relationships (correlation coefficients α and β) for different model parameters; hence a fully 3-D $\rho - v_S$ scaling relationship;
2. Through a slight modification of equation (3), the gradient of the relationship, α, is now inverted and optimized independently for each model parameter:

$$\alpha_m = (\mathbf{G}^T C_{gg}^{-1} \mathbf{G}(\boldsymbol{v}^0 + \Delta \mathbf{v}_m))^{-1} (\mathbf{G}^T C_{gg}^{-1} \mathbf{g}) \quad (4)$$

3. The $\mathbf{C}_{mm}$ matrix takes into account the error propagation from the velocity to the density model:

$$\sigma(\boldsymbol{\rho}_m) = \boldsymbol{v}_m \sigma(\alpha_m) + \alpha_m \sigma(\boldsymbol{v}_m) + \sigma(\beta_m) \quad (5)$$

where $\sigma(\boldsymbol{v}_m)$ is the seismic *a priori* model variance (0.05 km s^{-1}), weighted with the standard deviation associated with the path-averaged velocities, $\sigma(\alpha_m)$ and $\sigma(\beta_m)$ are the uncertainties in the coefficients of the scaling $\boldsymbol{\rho}_m$-$\boldsymbol{v}_m$ relationship. To control the amount of variation and to allow for correct changes in the parameter values, various tests were performed through the optimization process. The values on the main diagonal of $\mathbf{C}_{mm}$ (under the assumption that there is no correlation between the errors in each node) are chosen for an optimum trade-off between the data variance and the solution variance. Very small values of $\mathbf{C}_{mm}$ correspond to high values of C_{mm}^{-1}, hence representing over-regularized solutions where the density model remains close to the seismic model. Taking into account the *a posteriori* seismic standard deviation matrix (in Figure 4 (a)

are shown the mean diagonal elements); extensively analyzed in Maggi et al., 2006), higher $\sigma(\alpha_m)$ and $\sigma(\beta_m)$ uncertainties are assigned below a depth of 200 km (Figure 4 (b)). This enables the complementarity of the seismological and gravity data sets to be exploited, and reliable solutions to be obtained also below the seismic depth resolution.

As for our initial $v_{SVm}^0 - \rho_m^0$ relationship, we use a scaling profile derived from the empirical Birch's law (Birch, 1964). The widespread success of Birch's law can be ascribed to its virtual coincidence with, and hence linearization of, a power law derived from lattice dynamics over the density range ≈2.5–4.0 g/cm^3 (Chung, 1972), within which the rocks and minerals vary in our model. In addition, for our depths, the general trend of the pyrolite models (Cammarano et al., 2005), which are the best approximation of the composition of the Earth's upper mantle, does not differ much from the trend of the 1-D Birch relationship. Birch's law concerns P-wave velocities; our $v_{SVm}^0 - \rho_m^0$ depth-dependent relationships are the regression lines drawn through the plot of the two variables extracted from his tables. However, as studied by Simmons et al., (2009), a simple 1-D velocity-density scaling implies a direct relationship among seismic velocities, temperatures and density material. As this simplified view of density heterogeneity is clearly not correct, to account for additional dependencies on a wide range of factors, such as the presence of fluids or compositional variations, we allow the density-velocity scaling to vary laterally during the inversion, through (4), thus creating a fully 3-D relationship between the density and the shear-wave velocity model.

To proceed with the SII, we use the 3-D grid of our starting density model (ρ_m^0) to calculate the predicted gravity response **g** and the partial derivatives of each

gravity measurement $\mathbf{g}_n$ (where n are the [1,N] gravity observations) with respect to each density model parameter ρ_m:

$$\mathbf{G} = \left[\left(\frac{\partial g_n}{\partial \rho_m}\right)_{n.m}\right]^{NxM} \quad (6)$$

Residuals between the observed (Fig. 2 (b)) and the calculated gravity field ($\Delta\mathbf{g}$) are used as input for the inversion algorithm in (3). We then optimize the starting density-$\boldsymbol{v}_{SV}$ scaling relationships (α_m^0) and the starting density values (ρ_m^0), with (α_m^1) and $\Delta\rho_m^1$ (Figure 4 (c)) respectively.

At the same time, we calculate the gravity data misfit and the *a posteriori* standard deviation associated with the updated density parameters. The gravity data misfit is expressed as the *rms* of the gravity residuals for each observation:

$$rms = \sqrt{\frac{\sum_{n=1}^{N}\left(g_n^{obs} - g_n^i\right)^2}{N}} \quad (7)$$

where $\left(g_n^{obs} - g_n^i\right)$ is $\mathbf{\Delta g}$, as expressed above.

The *a posteriori* standard deviation associated with the updated density parameters ($\rho_m^i = \rho_m^{i-1} + \Delta\rho_m^i$), is calculated as:

$$\sigma\rho_m^i = \alpha_m^i \sigma v_{SVm}^{i-1} \left[1 - \left(Var(g(n)) \frac{d_{mm}}{\max(d_{mm})}\right)\right] \text{ (m=1,...M) (i=the current iteration)} \quad (8)$$

which is the propagation of uncertainty from the velocity to the density model, weighted with the final gravity variance reduction Var(g(n)), and the information provided by the gravity data (d_{mm} the diagonal elements of the gravity kernel $\left(G^T C_{gg}^{-1} G\right)$). The procedure is repeated, following the flow chart in Figure 3, until a satisfactory fit to the observed datasets (data misfit) is achieved. The higher the uncertainty in the input information, the lesser the number of iterations needed to obtain a model that satisfies both the datasets (however, usually not more

than 2–3 iterations).

2.3. Residual topography and mantle residual gravity anomalies

To recover the residual topography, the effects of the isostatic lithosphere are estimated with Panasyuk and Hager's (2000) algorithm and subtracted from the observed elevation (ETOPO1, Amante and Eakins, 2009). We assume that isostatic compensation is achieved within the lithosphere. Isostatic compensation can be achieved because both continental and young oceanic lithosphere essentially floats (mature oceanic lithosphere becomes increasingly denser than the asthenosphere and eventually sinks at subduction zones) on a relatively inviscid substrate (viscosity one order of magnitude lower than that of the upper mantle), i.e. the weak peridotite of the asthenosphere (Zhou, S., and Sandiford, M., 1992). Changes in the buoyancy or elevation of the lithosphere are accommodated by the displacement of the asthenospheric mantle in a finite length of time, related to its effective viscosity, in the order of 10^4-10^5 years. The association of the Earth's lithosphere with the upper cold thermal boundary layer of a convecting system (Schubert et al., 2001) enables us to select the depth of the lithosphere in our SII-ρ model. For each 1-D *xy* density depth profile we consider the depth recovered from Muller et al., (2008) isochrones as a guide, and we opportunely adjust the value in order to assign a depth point where we observe an inversion in the density gradient.

The mantle residual gravity anomalies are estimated as the differences between the gravity field produced by SII-ρ limited to the depth of the lithosphere and the observations.

Following the steps sketched in Figure 5, we estimate the correlation

matrix between the residual topography and the mantle residual gravity anomalies. We believe that a graphical representation of the diagonal values of this correlation matrix may be a proxy of the regions where the sublithospheric mantle density contributes to surface topography. We base our assumption on the papers of Pekeris (1935) and Richards and Hager (1984), which have shown that the viscous mantle flow that is driven by the thermal density contrasts is responsible for the long-wavelength gravity anomalies observed at the surface. They demonstrated that the gravitational effects of surface deformation caused by the thermally driven flow is opposite in sign and comparable in magnitude to that of the driving density contrast. It is therefore reasonable to expect that sublithospheric density contrasts have effects on the surface topography if a negative correlation is found between the residual topography and the mantle gravity residuals. This means that we can rule out compensations due to a low viscosity region at the base of the lithosphere.

3. RESULTS

Depth sections of the resulting SII-ρ density model, up to 300 km, after the first iteration, are plotted in Figure 6 (a) as a percentage deviation with respect to the mean model of each layer (Figure 6 (b)).

The optimization of the ρ-v_{SV} correlation coefficient in □3□□□enabled us to obtain the 3-D map of lateral variations in the angular coefficients of the ρ-v_{SV} coupling with respect to the 1-D thermal relationships (temperature variations are the dominant cause of density variations), and to select the regions characterized by density compositional signatures (Simmons et al., 2010, Tondi et al., 2012b). Figure 7 shows our interesting results. First of all compositional

variations presumably only affect to densities at the lithosphere-asthenosphere boundary (LAB), as chemically-induced density anomalies show up gradually from the Eastern to the North Western Pacific plate and do not extend below 200 km in depth. Additionally, important anomalies are observed mostly west of the East Pacific Rise (EPR) and are particularly emphasized at depth, beneath the northwestern part of the lithosphere.

The gravity data field reproduced by the resulting density model is shown in Figure 8. We obtain a gravity data misfit of 66.73 mgal (with respect to 321.16 mgal of the seismological model scaled into a density model) and a gravity data variance reduction of 67.41% (with respect to 31.58% of the seismic model). A comparison between the observed (Fig. 2 (b)) and the reproduced gravity data field (Fig. 8) evidences a good reproduction of the pattern of the Bouguer anomalies, with a uniform underestimation of densities within the Pacific Plate that is probably explained by the uncertainties in the recovered ρ-v_{SV} relationship (Figure 9) and that cannot affect our next inferences.

The *a posteriori* standard deviation, associated with the density parameters (Figure 10), ranges between 2.6 and 75.4 kg/m^3. Higher reliability of the density model, associated to smaller values of standard deviation, is obtained within the Pacific Plate, from 100 to 200 km depth. Further iterations do not improve the results, while they decrease the fit to the seismological data.

The identified thickness of the isostatic lithosphere in the Pacific plate ranges from 8 km in the EPR to 120 km depth in the Philippine Sea (Figure 11 (a), (b), (c)), including about 11 layers of the SII-ρ model.

The possibility to have available density information every 1°, enabled us to use detailed density profiles to calculate a) the differences between the

369 produced gravity field of the 3-D lithospheric density structure and the
370 observations, i.e. the mantle residual gravity and b) the isostatic height to be
371 subtracted from topography/bathymetry. Hence, we have tested the sensitivity
372 of both the calculated mantle residual gravity anomalies and the residual
373 topography to (i) the lithosphere depth uncertainty derived from the provided
374 standard deviation associated with the Müller et al., (2008) isochrones, and to
375 (ii) the chosen density model: the SII-ρ model (Figure 6 (a)) and the
376 seismological velocity model transformed into a density model through the
377 initial ρ-v_{SV} depth-dependent relationship.
378 The mantle residual gravity related to the SII-ρ model (Figure 11 (d), (e), (f)),
379 shows a negative anomaly characterizing the whole Pacific plate with a gradient
380 of 500 mgal between the eastern and the western coast. With regard to the SII
381 nonisostatic topography (Figure 11 (g), (h), (i)), it is characterized by general
382 positive values in the Pacific plate, which generally increase in the north-western
383 side and reach up to +3 km in the North West Pacific basin and in the Philippine
384 Sea. Important positive values are also found along the EPR. On the other hand,
385 continental regions are overcompensated.
386 Our sensitivity analysis shows that the variation in the depth of the lithosphere
387 (Figure 11 (a), (b) and (c)), as expected, particularly affects the residual gravity,
388 by lowering or increasing the mantle gravity residual anomalies (Figure 11 (d),
389 (e), (f)): a thinner lithosphere results in higher residual gravity anomalies. On the
390 other side, the residual topography associated with the Pacific plate (Figure 11
391 (g), (h), (i)) is slightly affected by the uncertainty associated with the depth of
392 the lithosphere, but the range of variations of the anomalies is more important
393 when considering a thicker lithosphere (Figure 11 (i)).

Mantle gravity residuals expressed by the SII-ρ model (Figure 12 (d), (e), (f)), are generally more negative with respect to those produced by the seismological model (Figure 12 (a), (b), (c)). Therefore this implies that SII-ρ model has a denser lithosphere, density increasing with depth, with a $\Delta\rho$ from 40 to 170 kg/m^3. As a consequence, residual topography associated to the seismic model (Figure 12 (d), (e), (f)) shows a stronger positive signature with an average Δh of 1.5 km.

The analysis of the negative correlation between the residual topography and the mantle residual gravity which, following Pekeris (1935) and Hager et al., (1985), should identify the regions where the contribution of mantle circulation in supporting the long-wavelength topography is active, enabled us to draw the pictures shown in Fig. 13 (a) to (f), for both the seismic and SII density models. Correlation is calculated for the *xy* grid of the 3-D model as:

$$d_p = \frac{(h_{res} - (\overline{h_{res}} + \sigma(h_{res}))}{(g_{res} - (\overline{g_{res}} + \sigma(g_{res}))} \quad (9)$$

where h_{res} is the residual topography and g_{res} is the mantle residual gravity, both weighted over the mean ($\overline{h_{res}}$ and $\overline{g_{res}}$) and the standard deviation ($\sigma(h_{res})$ and $\sigma(g_{res})$) in order to be comparable quantities. Fig. 5 shows the main steps we have followed to obtain our results.

As shown in Figure 13, the density model used in the calculation of (9) has a significant impact in determining the width of the area of the Pacific region affected by dynamic topography. If we use the density model directly transformed from the seismic model, the influence of mantle flow on the surface topography extends from the Peru-Chile trench to the Tonga trench in the South Pacific and from the west coast of the USA to the Philippine Sea in the North

418 Pacific (Figure 13 (a), (b), (c)). On the other hand, if we use the SII-ρ model, the
419 estimated contribution of mantle flow to the surface bathymetry is limited
420 mostly to the eastern side of the Pacific plate (Figure 13 (d), (e), (f)), and is more
421 consistent with the geoid lows (Figure 14). In addition, the lithospheric depth
422 uncertainties contribute in enlarging (when the lithospheric depth is smaller) or
423 reducing (when the lithospheric depth is greater) the region affected by dynamic
424 topography.
425 We wish to note that our results rely on a starting tomography model (Maggi et
426 al., 2006) which is undoubtedly limited by both spatial resolution and the used
427 methodology. However, as studied in Tondi and de Franco (2006), the interplay
428 with gravity information can efficiently constrain and complete the seismic
429 information. Additionally, the methodology enables us, through an assessment of
430 the gravity residuals, to become aware of the model inconsistencies. As
431 evidenced above, gravity residuals reproduced by SII-ρ model show a slight
432 uniform underestimation of densities beneath the Pacific Plate, that do not alter
433 the interdipendence among the different regions of the model, and as a
434 consequence, our inferences.
435
436 **4. DISCUSSION**
437
438 *4.1 The SII density model of the Pacific lithosphere and upper mantle*
439 The most prominent large-scale feature of the shallower pattern of
440 density anomalies, up to 150 km in depth (Figure 6 (a)), is a progressive increase
441 in density values across the Pacific plate from East to West, consistent with the
442 lithospheric age (Muller et al., 2008). At depth, as visualized with the help of

443 density isosurfaces (Figure 15), the high density/velocity anomaly reduces and is
444 gradually replaced by a uniform lower density anomaly which encompasses the
445 subsurface of all the plate. The reliability of these results is supported by the
446 calculation of the *a posteriori* standard deviation associated with the density
447 parameters (Figure 10), which evidences an excellent anomaly recovery in the
448 Pacific plate between depths of 100 and 200 km, where the model is well
449 constrained by both seismological and gravity information. This enables us to
450 evaluate, with confidence within that depth interval, both the recovered density
451 parameters and the deviation of the optimized angular coefficient of the ρ-v_{SV}
452 relationship, with respect to the a priori Birch coefficient.

453 Within the lithospheric depth, the progressive reduction of the positive
454 density anomaly (Fig. 6 (a)) correlates well with the increase of a chemically-
455 induced density anomaly (Fig. 7), which at 150 km depth becomes particularly
456 important beneath the northwestern part of the lithosphere and may help to
457 explain some inconsistencies between geodetical and seismological
458 observations. In fact, almost all seismological studies (Forsyth, 1977, Zhang and
459 Tanomoto, 1991, Maggi et al., 2006) show that lithospheric seismic velocities, the
460 thickness of the seismic lithosphere and the seismic velocities, in the low-
461 velocity zone below the lithosphere, all increase continuously with age when
462 averaged over isochrons, and do not flatten out for older lithosphere in the same
463 way that geoid and gravity observations do. Thus, the non-thermal density
464 anomalies at the base of the lithosphere may reduce the weight of the
465 lithosphere in that part of the model and explain the modest impact on the
466 gravity and geoid measurements.

467 Mid-ocean ridges, the western and the southern parts of North America

continent and the central Australian Proterozoic region below the Alice Springs Orogeny (Kennett and Iaffaldano, 2013) are characterized by negative density anomalies. Unlike the results of the tomographic inversion (Maggi et al., 2006), and in line with Dunn and Forsyth (2007), the negative density anomaly beneath the EPR is only slightly visible at shallower depths, becoming important between 200 and 250 km and disappearing at 300 km, thus confirming that convection is largely driven by cooling from above. No compositional contribution is observed from the analysis of the ρ-v_{SV} angular coefficient (Fig. 7), thus indicating that all anomalies are thermally induced heterogeneities. Positive density anomaly structures separated by negative density anomalies characterize the subsurface of convergent plate boundaries (Aleutian Trench, Mariana Trench, Kuril Trench, Kermadec Trench) and the subduction zones of Japan and Tonga-Kermadec, down to a depth of 300 km and below. The negative density anomalies probably reflect upward intrusions of arc magmas and/or fluids from hydrous partial melts in the mantle wedge. This is justified by the fact that the fluids control the pore fluid pressure and thus play an important role in the nucleation of interplate megathrust earthquakes, as well as large crustal earthquakes, which are typical in the arc and backarc areas (Zhao et al., 2002). At a depth of 200 km and below, positive density signatures of the continental cratons of Australia and North America are clearly visible.

In order to have a comprehensive insight of the contribution of the compositional heterogeneities to the overall density field of the Pacific plate, and extrapolate the contribution of the gravity data to the seismic model, the recovered SII density values have been plotted against the seismological shear velocities (Figure 9). It is evident that the general trend of the SII ρ-v_{SV}

493 relationships follows the 1-D Birch relationships, which is the same as the
494 general agreement between the upper mantle density anomalies and the velocity
495 structures observed by the tomographic inversion of Maggi et al., (2006).
496 However, the SII optimization procedure increases the value of the a priori
497 α coefficient (the gradient of the ρ-v_{SV} relationship), within the limits of 10% -
498 40% that, with the help of Figure 7, we localize to the parameters that belong to
499 the oceanic lithosphere and to the upper mantle structures below the Pacific
500 plate. These results are consistent with the findings of Simmons et al., (2009) of a
501 positive residual density anomaly beneath the eastern Pacific Ocean extending
502 from Antarctica to Alaska, which does not have a thermal origin. Lowered scaling
503 factors are observed within and below the continental lithosphere, but in this
504 case, higher values of the a posteriori standard deviation suggest us to evaluate
505 this result with caution.

506 As a result of the general increase in density parameters related to the
507 area of the Pacific plate, our 1-D mean density model, unlike the starting 1-D
508 ρ model directly transformed from seismic data, is higher than PREM between
509 50 and 220 km (Fig. 6 (b)). The contribution of gravity information, may have
510 corrected the density values that are linked to observations with primary
511 sensitivity to v_{SV} (e.g. the Rayleigh waves) that, as observed by Ekström and
512 Dziewonski (1998), in the presence of an underestimated radial anisotropy
513 anomaly beneath the Pacific plate, are of significant smaller amplitude, with
514 respect to parameters obtained from observations with primary sensitivity to
515 v_{SH} (e.g. Love waves).

516

517 *4.2. The mantle residual gravity anomalies and the residual topography of the*

518 *Pacific Plate*

519 As discussed in McNutt (1998), the high viscosity of the plates may shield
520 surface geologic processes from convective forces below and explain the
521 deviations of ocean depth or seafloor topography from the prediction of a cooling
522 half-space model. As a result, the residual topography (Figure 11 (g), (h), (i) and
523 Figure 12 (d), (e), (f)), which is estimated on the basis of the isostatic height and
524 the density within and beneath the lithosphere, would have a marginal
525 contribution compared to the mantle gravity residuals (Figure 11 (d), (e), (f) and
526 Figure 12 (a), (b), (c)) which depend on the deeper density anomalies. As this is
527 what we observe, we presume that the imbalance between the intensities of
528 mantle gravity residuals and the residual topography, which we observe
529 especially for the SII-ρ model, is due to a lateral viscosity growth, associated with
530 the increasing thickness and density of the Pacific Plate, from the EPR towards
531 west, up to the Kermadec and Tonga Trench in the south and the Kuril-
532 Kamchatka Trench in the north (Figure 6 and Figure 15). However, although in
533 the Northwestern Pacific the surface uplift is presumably shallower than the
534 mantle upwelling, because it only compensates for a part of the mass deficit, this
535 occurrence does not explain the conjunction of anomalous height of seafloor
536 topography, the lack of a heat flow anomaly and the net geoid low observed in
537 the regions around the Hawaiian Swell and South Pacific Super Swell (Figure 14).

538 Following McNutt (1998) and Mc Nutt and Bonneville (2000), who
539 suggested that the discrepancy between the heat flow and depth of the
540 lithosphere could imply that the origin of the Super Swell is non-thermal (e.g. the
541 convecting material beneath is low density by virtue of its mineralogy rather
542 than its temperature), we use our results on the optimization of the ρ-v_{SV}

543 correlation coefficient (Fig. 7) to test this hypothesis. On the basis of our results,
544 Mc Nutt's hypothesis is plausible, as chemically-induced density anomalies can
545 be observed all along subducting slabs, beneath both the Hawaiian and the South
546 Pacific Super Swell, and in the structure of the lithosphere between the Aleutian
547 Trench and the Fiji North Plateau in the northwestern edge of the Plate. These
548 observations are also justified by the fact that perturbed phase relations among
549 mantle minerals are expected within the thermal environment of subducting
550 slabs (Bina et al., 2001). In addition, the compositionally-induced density
551 anomaly beneath the surface of both the Swells, may explain why the measured
552 average heat flow is not resolvably different from other Pacific values, in spite of
553 the presence of the topographic highs.
554 With regard to the geoid (Fig. 14), a semi continuous belt of lows surrounds the
555 Pacific, including isolated minima in the Indian Ocean, Ross Sea and northeast
556 Pacific. No corresponding negative anomalies are observed in the free-air and/or
557 Bouguer gravity map and, as a consequence, no information is given by our study
558 in this regard. As studied by Spasojevic et al., (2010), the geoid lows are
559 correlated with high-velocity anomalies near the base of the mantle and low-
560 velocity anomalies in the mid-to-upper mantle, hence they are not constrained
561 by our density model.
562 A mass deficit up to depth of 150 km (Fig. 6), correlated with calculated positive
563 residual topography (Fig. 11 g), h), i)) and observed positive geoid anomaly (Fig.
564 14) is instead reconstructed by our model beneath the Hawaiian chain.
565 Following Cadio et al., (2012) the average depth of the compensating density
566 anomaly, might indicate compensation within the asthenosphere such as by
567 dynamic uplift, which is unfortunately not confirmed by our proxy of dynamic

568 topography (Fig. 13). On the contrary, we are in favor of the presence of crustal
569 underplating, that, as suggested by Leahy et al., (2010), and previously identified
570 by the deep-penetrating marine refraction study of Watts et al., (1985) indicates
571 that the Hawaiian Swell is partially supported by shallow chemical buoyancy
572 which can be conveniently associated to the recovered compositional anomaly
573 (Fig. 7).
574 The geoid in the Super-Swell region, that following Adam and Bonneville (2004)
575 covers an area between latitudes 10°N and 30°S and longitudes [130-160]°W,
576 shows two different features: a positive anomaly in the northern branch, that
577 becomes progressively negative towards the South. Correlated positive to
578 negative density anomalies are reconstructed up to 100 km depth and below the
579 lithosphere (Fig. 15). The analysis of the negative correlation between the
580 residual topography and the mantle residual gravity evidences that in this region
581 is active the contribution of mantle circulation in supporting the long-
582 wavelength topography. This is particularly evident with the seismic model. With
583 the SII model, the mantle support is of limited amplitude and more relevant in
584 the northern part of the Swell (Fig. 13). As studied by Adam et al., (2014)
585 dynamic topography is sensitive both to the viscosity profile and to the
586 tomographic models. As suggested above, results support the presence of a
587 lateral viscosity growth, associated with the increasing thickness of the Pacific
588 plate. Hence we favor the presence of a low viscosity asthenosphere beneath the
589 South Pacific superswell, accordingly to the study of Adam et al., (2014). The
590 presence of density compositional variations reduces the negative correlation
591 between residual topography and the mantle residual gravity and this explains
592 the differences of the results obtained with the seismic and the SII models.

593 Density compositional variations, especially important in the Southern branch of
594 the Swell, are also consistent with the hypothesized underplating beneath the
595 Marquesas swell (McNutt and Bonneville, 2000). Surface topography of the
596 Superswell region may then by explained by the joint contribution of dynamic
597 topography and crustal underplating which offers another source for the
598 buoyancy of the Swell and justifies the measured heat flow (Veselov and Lipina,
599 1982), which is not resolvably different from other Pacific values.
600

601 **3. CONCLUSIONS**

602 The exploitation of the information provided by the seismological and
603 satellite gravity data, enabled us to contribute to the determination of important
604 physical and geological information within the lithospheric and upper mantle
605 structure of the Pacific, down to 300 km depth.
606 The recovered parameters on a uniform 1° x 1° grid , such as 1) the densities
607 compatible with both seismological and gravity observations and 2) the phase
608 relationships between the isotropic shear-wave velocity and the density
609 structure enabled us to extract useful and novel information on a) the thickness
610 of the lithosphere, b) the thermally and chemically-induced density anomalies, c)
611 the residual topography, d) the mantle gravity residuals, e) the dynamic
612 topography and f) midplate swells for the whole Pacific region. This information
613 should help to reconcile some incompatible descriptions of the oceanic
614 lithosphere of the Pacific.
615 Unlike the results of tomographic inversion, the negative density anomaly
616 beneath the EPR are chemically induced at shallower depths, thus confirming
617 that the overall upwelling is passively driven by plate motions. Additionally, with

618 respect to the seismological studies, we observe that 1) the SII-ρ model shows a
619 lighter lithosphere, 2) a wide area of strong positive densities strengthened by
620 strong negative chemically-induced density anomalies is revealed between the
621 Aleutian Trench and the Fiji Plateau in the northwestern edge of the Pacific plate,
622 3) both the Hawaiian and the Super Swell are characterized by density
623 compositional variations that may support the hypothesized crustal
624 underplating, 4) the proxy of the contribution of mantle flow to the surface
625 bathymetry is concentrated beside the western flank of the EPR and decreases
626 progressively towards the western Pacific Plate, 5) the features of the recovered
627 mantle gravity residuals evidence a lateral viscosity growth, associated with the
628 increasing thickness of the Pacific Plate, from the EPR towards west, up to the
629 Kermadec and Tonga Trench in the south and the Kuril-Kamchatka Trench in the
630 north.
631 From these results, we conjecture that the cooled layer of mature lithosphere
632 thickens with age as suggested by the dispersion of Rayleigh waves with oceanic
633 paths (Zhang and Tanimoto, 1991. Maggi et al., 2006). However, from a depth of
634 70 to 150 km, pressures and temperatures chemically modify the composition of
635 the lithospheric layer. This chemically-modified structure is lighter and more
636 buoyant than the predicted cooling models, which reconciles gravity
637 observations that do not show an increasing gradual negative gradient
638 progressing towards the north-western side of the Plate. In addition, the
639 existence of non-thermal sources of buoyancy at the base of the lithosphere,
640 below the northwestern side and along the eastern boundary of the Pacific plate,
641 also justifies the fact that the conducted heat flux stabilizes to a constant value of
642 50 to 60 $\frac{W}{Km}$ after 25 or 30 million years (Stein, 1995) and does not vary

643 significantly compared to other Pacific values, although the depth is different.
644 Presumably, after this time, phase relations among mantle minerals start to be
645 perturbed and the direct relationship between the convective material beneath
646 and its temperature is progressively lost. Coherently with the observed
647 chemically modified structures, results support also the hypothesis that midplate
648 swells are not entirely explained by thermal and dynamic surface uplift from
649 rising mantle plumes, but by a joint contribution of volcanic underplating and
650 mantle flow.
651

652 **Aknowledgments**

653 The results in this paper were obtained thanks to the CINECA Italian
654 SuperComputing Resource Allocation (ISCRA) HP10CNWW73 and HP10CJNYL3.
655 A special thank of the authors to Dr. A. Maggi for supplying data and information
656 related to the seismological model.
657

658 **REFERENCES**
659

660 Adam, C., Bonneville, A., 2004. Extent of the South Pacific Superswell, Journ. of
661 Geophys. Res., 110, B09408, doi: 10.1029/2004JB003465

662

663 Adam C., Yoshida M., Suetsugu D., Fukao Y., Cadio C., 2014. Geodynamic
664 modeling of the South Pacific superswell. PEPI, 229, 24-39, doi:
665 10.1016/j.pepi.2013.12.014

666

667 Afonso, J.C., Zlotnik, S., Fernandez, M., 2008. The effects of compositional and
668 rheological stratifications on small-scale convection under the oceans:
669 implications for the thickness of oceanic lithosphere and seafloor flattening.
670 Geophys. Res. Lett. 35, L20308, doi:10.1029/2008GL035419.

671

672 Amante, C., Eakins, B.W., 2009. ETOPO1 1 Arc-Minute Global Relief Model:
673 Procedures, Data Sources and Analysis. NOAA Technical Memorandum NESDIS
674 NGDC-24. National Geophysical Data Center, NOAA. doi:10.7289/V5C8276M

675

676 Bina, C.R., Stein, S., Marton, F.C., Van Ark, E.M., 2001. Implication of slab
677 mineralogy for subduction dynamics, Physics of the Earth and Planetary
678 Interiors, 127, 51-66.

679

680 Birch, F., 1964. Density and composition of mantle and core, J. Geophys. Res.,
681 69(20), 4377–4384.

682

683 Blakely, R.J., 1995. Potential Theory in Gravity and Magnetic Applications,
684 Cambridge Univ. Press, New York.

685

686 Boschi, L., Faccenna, C., Becker, T.W., 2010. Mantle structure and dynamic
687 topography in the Mediterranean Basin. Geophys. Res. Lett., 37, L20303,
688 doi.10.1029/2010GL045001.

689

690 Cadio, C., Ballmer, M.D., Panet, I., Diament, M., Ribe, N., 2012. Constraints on the
691 origin of the Hawaiian swell from wavelet analysis of the geoid to topography

ratio, EPSL, 359-360, 40-54.

Cammarano, F., Deuss, A., Goes, S., Giardini, D., 2005. One dimensional physical reference models for the upper-mantle and transition zone: Combining seismic and mineral physics constraints, J. Geophys. Res., 110, B01306, doi:10.1029/2004JB003272.

Caratori Tontini, F., Graziano, F., Cocchi, L., Carmisciano, C., Stefanelli, P., 2007. Determining the optimal Bouguer density for a gravity data set: Implications for the isostatic setting of the Mediterranean Sea. Geophys. J. Int., 169, 380–388.

Chung, D.H., 1972. Birch's law: Why is it so good?, Science, 177, 261–263.

Dávila, F., Lithgow-Bertelloni, C., 2013. Dynamic topography in South America. Journal of South American Earth Sciences, 43, 127-144.

Drinkwater, M.R., Floberghagen, R., Haagmans, R., Muzi, D. and Popescu, A., 2003. GOCE: ESA's first Explorer Core mission. Space Science Reviews, 108, 419-432.

Dunn, R.A., Forsyth, D.W., 2007. Crust and lithospheric structure – Seismic structure of Mid-Ocean Ridges. In Treatise of Geophysics, Elsevier, ISBN: 978-0-444-52748-6, pp 419-443.

Doin, M.P., Fleitout, L., 2000. Flattening of the oceanic topography and geoid: Thermal versus dynamic origin. Geophysical Journal International, 143, 582-594.

717

718 Dziewonski, A.M., Anderson, D.L., 1981. Preliminary reference Earth model, Phys.
719 Earth Planet. Inter., 25, 297–356.

720

721 Ekstrom, G., Dziewonski, A.M., 1998. The unique anisotropy of the Pacific upper
722 mantle, Nature, 394, 168-172.

723

724 Forsyth, D., 1977. The evolution of the upper mantle beneath mid-ocean ridges,
725 Tectonophysics, 38**,** 89–118.

726

727 Forte, A.M., 2007. Constraints on seismic models from other disciplines —
728 implications for mantle dynamics and composition. In: Romanowicz, B.,
729 Dziewonski, A.M. (Eds.), Volume 1 of Treatise of Geophysics. Elsevier, pp. 805–
730 858.

731

732 Flament, N., Gurnis, M., Müller, R.D., 2013. A review of observations and models
733 of dynamic topography. Lithosphere, 5, (2), 189-210.

734

735 Gilardoni, M., Reguzzoni, M., Sampietro, D., Sansò, F., 2013. Combining EGM2008
736 with GOCE gravity models. Bollettino di Geofisica Teorica e Applicata, 54 (4),
737 285-302.

738

739 Heiskanen, W.A., Moritz, H., 1967. Physical Geodesy. Freeman, San Francisco.

740

741 Jarvis, G.T., Peltier, W.R., 1982. Mantle convection as a boundary layer
742 phenomenon. Geophysical Journal of the Royal Astronomical Society, 68, 385-
743 424.

744

745 Kido, M., Seno, T., 1994. Dynamic topography compared with residual depth
746 anomalies in oceans and implications for age-depth curves. Geoph. Res. Lett., 21,
747 717-720.

748 Kozlovskaya, E., Janik, T., Yliniemi, J., Karateyev, G., Grad, M., 2004. Density-
749 velocity relationship in the upper lithosphere obtained from P- and S-wave
750 velocity models along the Eurobridge'97 seismic profile and gravity data, Acta
751 Geophys. Pol., 52(4), 397–424.

752

753 Leahy, G.M., Collins, J.A., Wolfe, C.J., Laske, G., Solomon, S.C., 2010. Underplating of
754 the Hawaiian Swell: evidence from teleseismic receiver functions, Geoph. J. Int.,
755 183, 313-329.

756

757 Maggi, A., Debayle, E., Priestley, K., Barruol, G., 2006. Multimode surface
758 waveform tomography of the Pacific Ocean: a closer look at the lithospheric
759 cooling signature. Geophys. J. Int., 166, 1384–1397, doi: 10.1111/j.1365-
760 246X.2006.03037.x.

761

762 Mayer-Gürr, T., 2006. Gravitationsfeldbestimmung aus der Analyse kurzer
763 Bahngen am Beispiel der Satellitenmissionen CHAMP und GRACE (PhD thesis).
764 University of Bonn, Germany.

765

766 McKenzie, D.P., 1967. Some remarks on heat flow and gravity anomalies, J.
767 Geophys. Res., 72(6), 261–266, 273.

768

769 McNutt, M.K, Bonneville, A., 2000. A shallow, chemical origin for the Marquesas
770 swell. Geochemistry Geophysics Geosystems, Vol. 1, 6, DOI:
771 10.1029/1999GC000028

772

773 McNutt, M.K., 1998. Superswells. Reviews of Geophysics, 36 (2), 211-244.

774

775 Müller, R.D., Sdrolias, M., Gaina, C., Roest, W.R., 2008. Age spreading rates and
776 spreading asymmetry of the world's ocean crust. Geochemistry, Geophysics,
777 Geosystems, 9, Q04006, doi:10.1029/2007GC001743.

778

779 Nataf, H.C., Ricard, Y., 1996. 3SMAC: an a priori tomographic model of the upper
780 mantle based on geophysical modelling, Phys. Earth Planet. Inter., 95, 101– 122,
781 doi:10.1016/0031-9201(95)03105-7.

782

783 Pail, R., Bruinsma, S., Migliaccio, F., Förste, C., Goiginger, H., Schuh, W.D., Höck, E.,
784 Reguzzoni, M., Brockmann, J.M., Abrikosov, O., Veicherts, M., Fecher, T.,
785 Mayerhofer, R., Kransbutter, I., Sansò, F., Tscherning, C.C., 2011. First GOCE
786 gravity field models derived by three different approaches. J. Geod., 85(11), 819-
787 843.

788

789 Panasyuk, S.V., Hager, B.H., 2000. Models of isostatic and dynamic topography,
790 geoid anomalies, and their uncertainties, J. Geophys. Res., 105, B12, 28, 199–
791 28,209.
792
793 Pavlis, N.A., Holmes, S.A., Kenyon, S.C., Factor, J.K., 2012. The development and
794 evaluation of the Earth Gravitational Model 2008 (EGM2008). J. Geophys. Res.,
795 117, B4.
796
797 Parker, R., Oldenburg, D., 1973. Thermal model of ocean ridges, Nature, 242,
798 137–139.
799
800 Pekeris, C.L., 1935. Thermal convection in the interior of the Earth, Geophys. J.
801 Int., 3, 343–367, doi:10.1111/j.1365-246X.1935.tb01742.x.
802
803 Richards, M.A., Hager, B.H., 1984. Geoid anomalies in a dynamic Earth, J. Geophys.
804 Res., 89, 5987–6002.
805
806 Simmons, N.A., Forte, A.M., Grand, S.P., 2009. Joint seismic, geodynamic and
807 mineral physical constraints on three-dimensional mantle heterogeneity:
808 Implications for the relative importance of thermal versus compositional
809 heterogeneity, Geophys. J. Int., 177, 1284-1304.
810
811 Simmons, N.A., Forte, A.M., Boschi, L., Grand, S., 2010. GyPSuM: A joint
812 tomographic model of mantle density and seismic wave speeds, J. Geophys. Res.,
813 115, B12310, doi:10.1029/2010JB007631.

814

815 Smith, W.H.F., Sandwell, D.T., 1997. Global sea floor topography from satellite
816 altimetry and ship depth soundings. Science, 277, 1956-1962.

817

818 Stein, C.A., 1995. Heat flow from the Earth. In Ahrens T.J., Global Earth Physics, A
819 Handbook of Physical Constants, Washington, AGU.

820

821 Schubert, G., Turcotte, D.L., Olson, P., 2001. Mantle Convection in the Earth and
822 Planets, Cambridge University Press, Cambridge.

823

824 Spasojevic, S., Gurnis, M., Sutherland, R., 2010. Mantle upwellings above slab
825 graveyards linked to the global geoid lows, Nature Geoscience, 3, 435-438.

826

827 Stein, C.A., Stein, S., 1992. A model for the global variation in oceanic depth and
828 heat flow with lithospheric age. Nature 359, 123.

829

830 Tondi, R., de Franco, R., Barzaghi, R., 2000. Sequential integrated inversion of
831 refraction and wide-angle reflection traveltimes and gravity data for two-
832 dimensional velocity structures. Geophys. J. Int., 141, 679-698, doi:
833 10.1046/j.1365-246x.2000.00104.x

834

835 Tondi, R., Cavazzoni, C., Morelli, A., 2012a. Parallel “large” dense matrix
836 problems: Application to 3D joint inversion of seismological and gravity data.
837 Comput. Geosci., 48, 143-156, doi:10.1016/j.cageo.2012.05.026.

838

839 Tondi, R., de Franco, R., 2006. Accurate assessment of 3D crustal velocity and
840 density parameters: Application to Vesuvius data sets. Phys. of the Earth and
841 Plan. Int., 159, 183-201.

842

843 Tondi, R., Schivardi, R., Molinari, I., Morelli, A., 2012b. Upper mantle structure
844 below the European continent: Constraints from surface-wave tomography and
845 GRACE satellite gravity data. J. geophys. Res., 117, B09401,
846 doi:10.1029/2012JB009149.

847

848 Veselov, O.V., and Lipina, E.N., 1982. Catalogue of heat flow data from East of
849 Asia, Australia and West Pacific Ocean, World Data Center for Solid Earth
850 Physics.

851

852 Watts, A.B., Ten Brink U.S., Buhl P, and Brocher T.M., 1985. A Multichannel
853 seismic study of lithospheric flexure across the Hawaiian-Emperor seamount
854 chain, Nature 315, 105-111.

855

856 Zhang, Y.S., Tanimoto, T., 1991. Global Love wave phase velocity variation and its
857 significance to plate tectonics. Phys. Earth Planet. Inter., 66, 160-202.

858

859 Zhang, N., Zhong, S., Flowers, R.M., 2012. Predicting and testing continental
860 vertical motion histories since the Paleozoic. Earth and Planetary Science Letters,
861 317–318, 426–435, doi:10.1016/j.epsl.2011.10.041.

Zhao, D., Mishra, O., Sanda, R., 2002. Influence of fluids and magma on earthquakes: seismological evidence. Phys. Earth planet. Inter., 132, 249–267.

Figure captions

Fig. 1. Latitude-dependent standard deviation of the GOCE-only model commission error [mgal].

Fig. 2: (a) Free-air gravity anomalies from 128,880 points of the combined GOCE-EGM2008 model over the study area (degree 2190). b) Bouguer anomaly map of the Pacific Plate recovered from (a). See paragraph 2.1 for details.

Fig. 3. Flow chart of the inversion procedure, including optimization of density and velocity.

Fig. 4. Comparison among (a) the mean diagonal elements of the *a posteriori* seismic standard deviation, (b) the assigned mean diagonal elements of the C_{mm} covariance matrix (takes in account the error propagation from the velocity model to the density model and (c) the mean density update of the first iteration ($\Delta\rho^1$)

Fig. 5. Sketch of the followed steps to recover (d) the diagonal values of the correlation matrix between the residual topography and the mantle residual gravity anomalies produced by the SII density model. As an example, (a) a

887 vertical slice through the recovered model (30° N) is analyzed. The method used
888 to determine the depth of the lithosphere is explained in the text. Following
889 Pekeris (1935) and Hager et al., (1985), (d) the negative correlation between (b)
890 the mantle residual gravity anomaly and (c) the residual topography, may
891 identify the regions where the contribution of mantle circulation in supporting
892 the long-wavelength topography is active.
893
894 Fig. 6. Depth sections of the ρ percentage perturbations in (a) our optimized SII-
895 ρ model. Model perturbations are expressed as percentage deviations with
896 respect to (b) the mean density value of each layer. In each section, the main
897 tectonic units are indicated. In (b) the depth interval of the lithosphere in 1-D SII-
898 ρ, PREM and seismic model (Maggi et al., 2006) are shown. The area of the
899 Pacific Superswell, identified by Adam and Bonneville (2005), is superimposed
900 on each section.
901
902 Fig. 7. Depth sections of the lateral differences in the optimized angular
903 coefficient α with respect to the a priori Birch coefficients (0.72 for 50 km depth,
904 0.34 from 100 to 200 km depth). The area of the Pacific Superswell, identified by
905 Adam and Bonneville (2005), is superimposed on each section.
906
907 Fig. 8. Bouguer anomaly map reproduced by SII-ρ model in Fig. 6 (a). Gravity
908 misfit with respect to observations in Fig. 2 (b) is 66.73 mgal and variance
909 reduction is 67.4%.
910

911 Fig. 9. Density values from the recovered SII-ρ model in Fig. 6(a), plotted against
912 the velocity values from the seismological model and compared to Birch law
913 regression lines (black solid lines), our $v_{SVm}^0 - \rho_m^0$ starting relationship .
914
915 Fig. 10. Depth sections of *a-posteriori* percentage standard deviation on SII-
916 ρ model. Standard deviation takes into account the propagation of uncertainty
917 from the velocity to the density model, weighted with the final gravity variance
918 reduction Var(g(n)), and the information given by the gravity data (eq. (8)). In
919 each section, the standard deviation values are referred to the 1-D SII-ρ model,
920 imaged in Fig. 6 (b). In the first section, the main tectonic units are indicated.
921
922 Fig. 11. (a), (b) (c) Calculated lithospheric thickness of the Pacific region, derived
923 mostly from Müller et al., (2008) isochrones (see text for additional information).
924 (b) shows the mean value and (a) and (c) show the mean value minus and plus
925 the standard deviation respectively. (d),(e),(f) Mantle residual gravity anomalies
926 (background density is adjusted in order to magnify the contrast between ocean
927 and continents) calculated assuming the SII density model and the lithospheric
928 depth in (a), (b) and (c).
929 (g), (h), (i) Residual topography of the Pacific region, calculated assuming the SII-
930 ρ density model and the lithospheric depth in (a), (b) and (c).
931 The area of the Pacific Superswell, identified by Adam and Bonneville (2005), is
932 superimposed on each section.
933
934 Fig. 12. (a), (b) (c) Mantle residual gravity anomalies calculated assuming that
935 the seismic model has been transformed into a density model through the

936 starting ρ-vSV depth-dependent relationship and the lithospheric depth in Fig.
937 11 (a), (b) and (c).
938 (d), (e), (f) Residual topography of the Pacific region, calculated assuming the
939 seismic model transformed in a density model through the starting ρ-vSV depth-
940 dependent relationship and the lithospheric depth in Fig. 11 (a), (b) and (c).
941 The area of the Pacific Superswell, identified by Adam and Bonneville (2005), is
942 superimposed on each section.
943
944 Fig. 13. (a), (b), (c) Proxy of dynamic topography for the seismic model
945 transformed in a density model through the starting ρ-vSV depth-dependent.
946 (d), (e), (f) Proxy of dynamic topography for the SII-ρ model. Contour plots
947 highlight the areas of negative relationship between the residual topography
948 (subtracted by mean + standard deviation) and the mantle residual gravity
949 (subtracted by mean + standard deviation) of the Pacific region. The area of the
950 Pacific Superswell, identified by Adam and Bonneville (2005), is superimposed
951 on each section.
952
953 Fig. 14. Geoid undulations from the combined GOCE-EGM2008 model over the
954 study area. Minimum value is -68,47 m, maximum value is 87,36 m. The area of
955 the Pacific Superswell, identified by Adam and Bonneville (2005), is
956 superimposed. The main tectonic units are indicated.
957
958 Fig. 15. Isosurfaces of densities characterizing the structures of the upper mantle
959 below the Pacific region as seen (a) directly overhead and in a 3-D view (b) cut
960 from 50 km depth, (c) cut from 150 km depth, (d) cut from 250 km depth.

961 Earthquakes from ISC and NEIC catalogues are shown as blue stars for
962 magnitudes between 7.0 and 7.5 and as black circles and as black circles for
963 magnitude greater than 7.5. The area of the Pacific Superswell, identified by
964 Adam and Bonneville (2005), is superimposed on each plot.
965
966

Figure 1

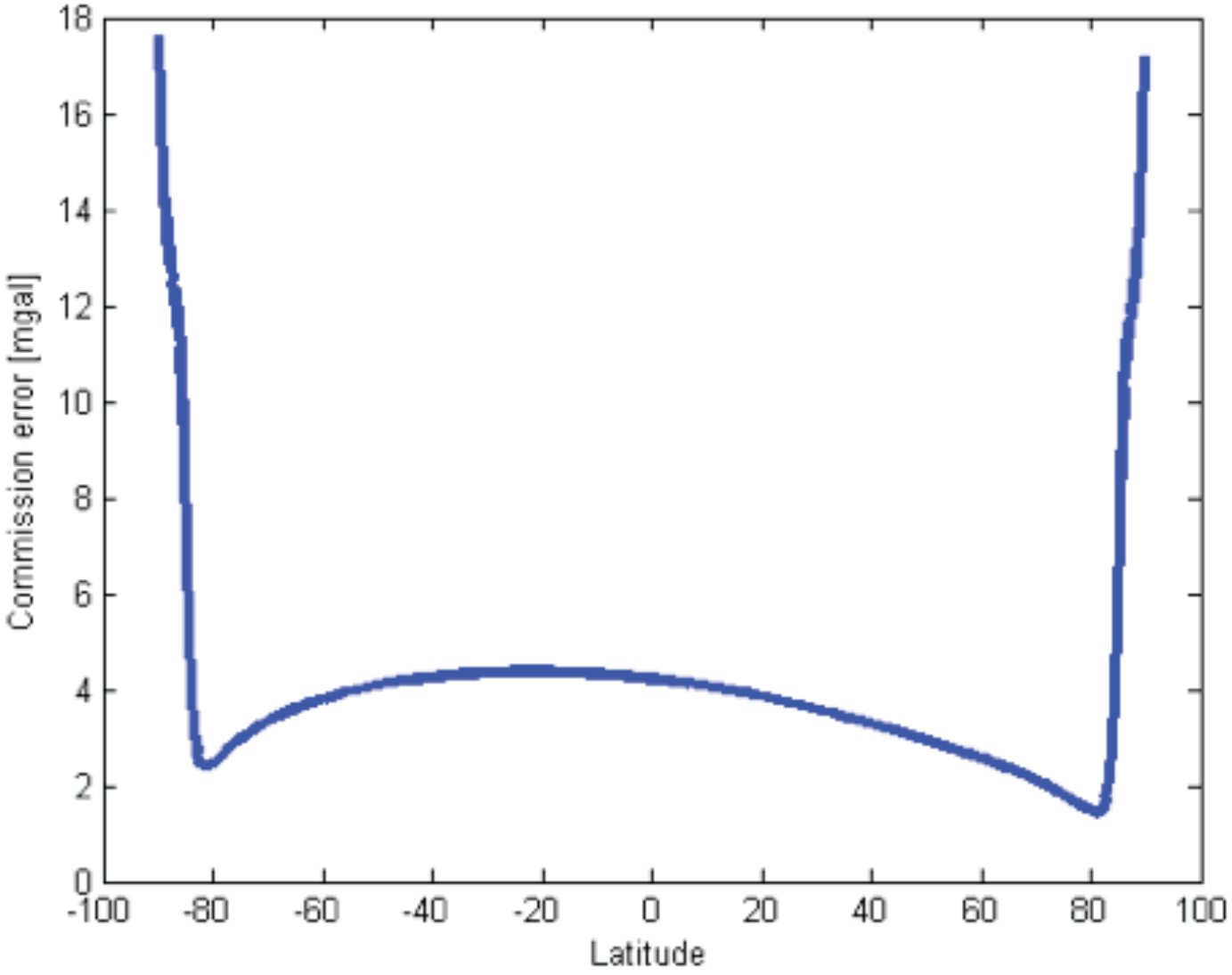

Fig. 1: Latitude-dependent standard deviation of the GOCE-only model commission error [mgal]

Figure 2

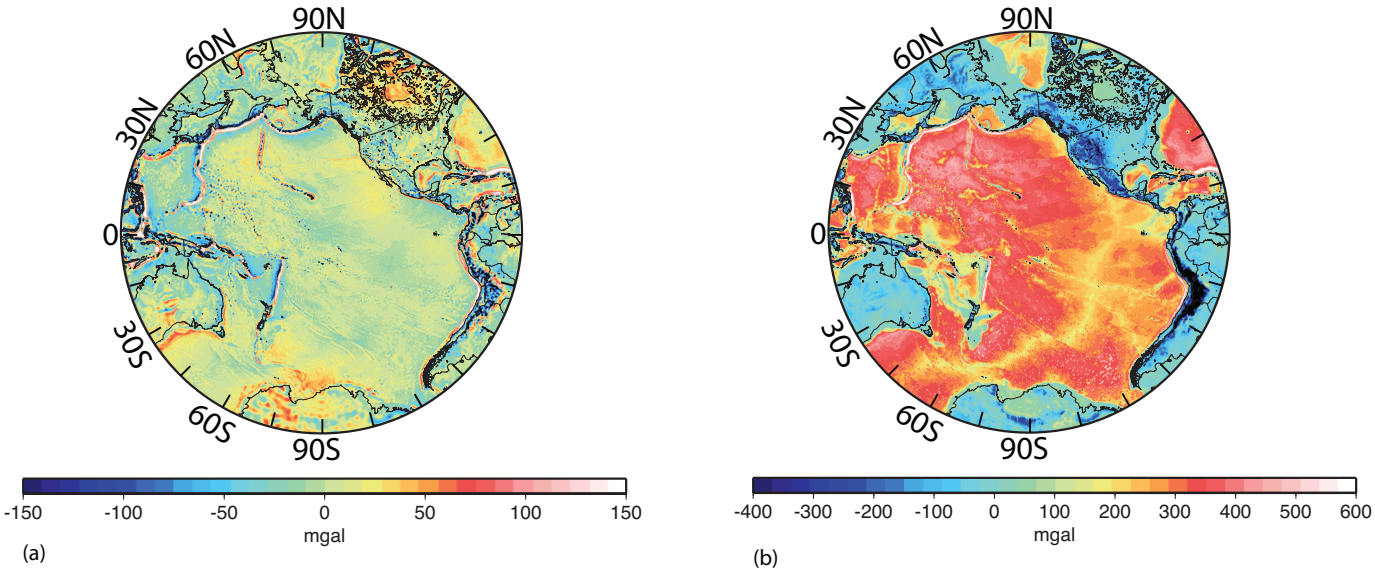

Fig. 2. (a) Free-air gravity anomalies from 128,880 points of the combined GOCE-EGM2008 model over the study area (degree 2190). (b) Bouguer anomaly map of the Pacific Plate recovered from (a). See paragraph 2.1 for details.

Figure 3

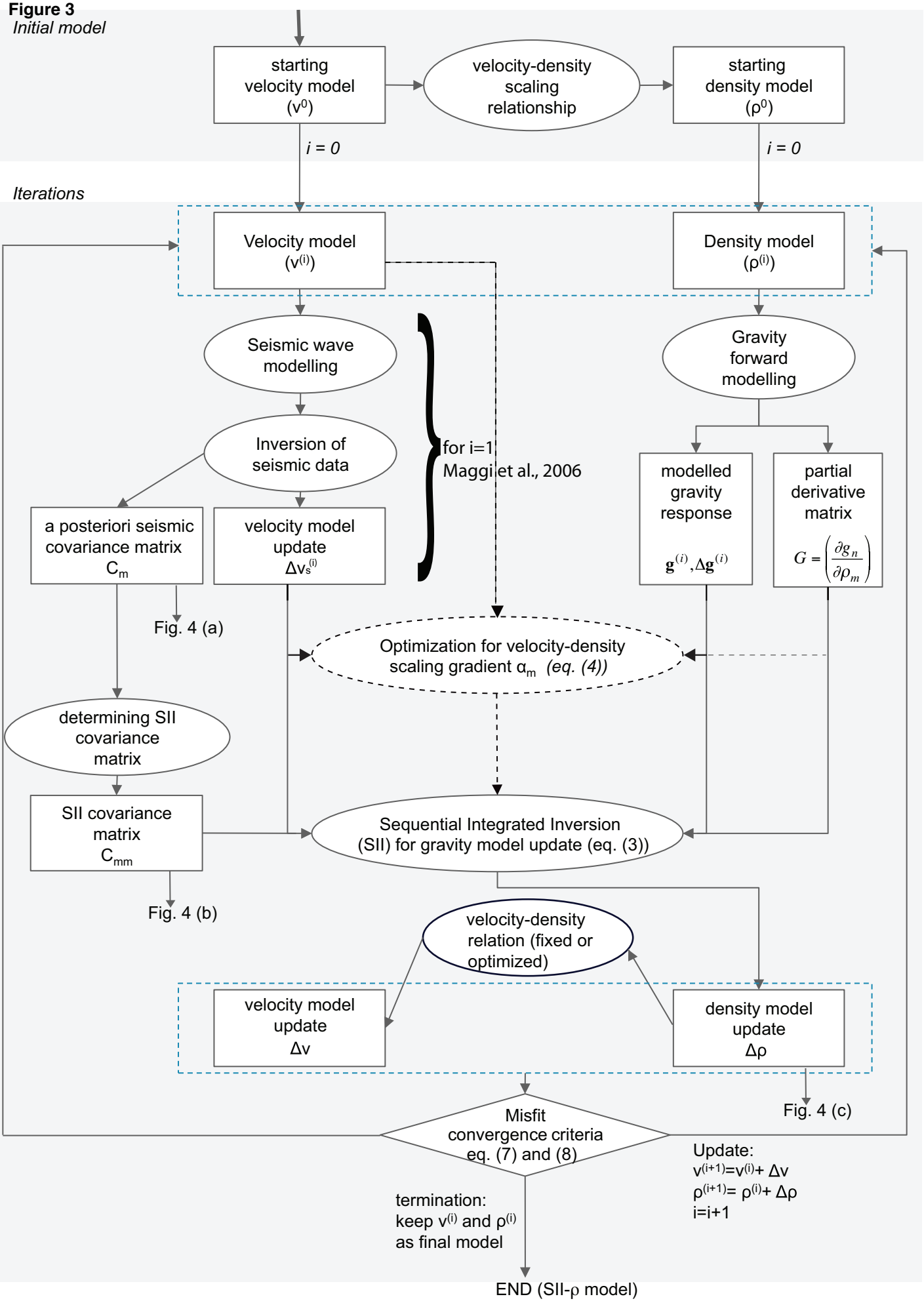

Fig. 3. Flow chart of the inversion procedure, including optimization of density and velocity.

Figure 4

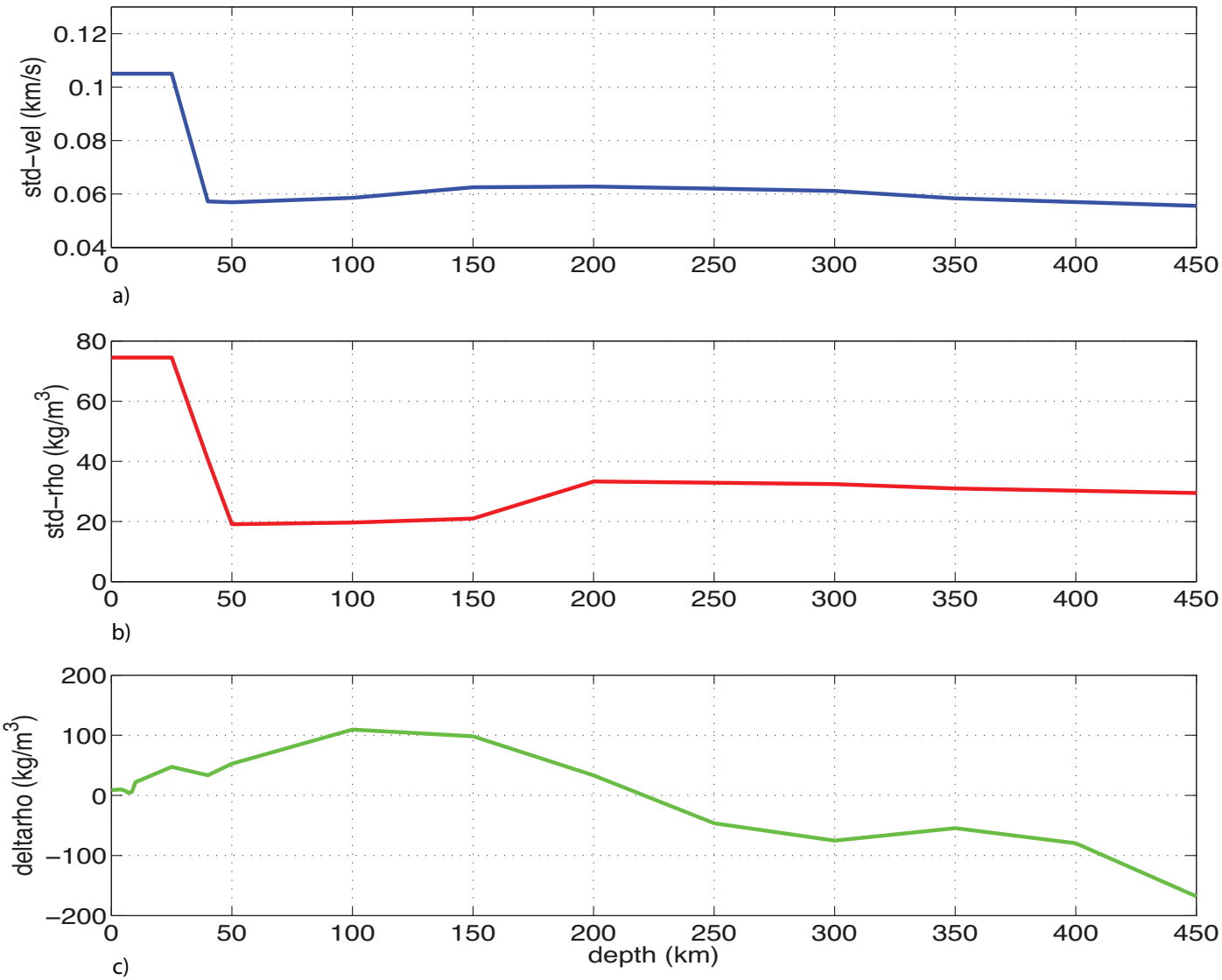

Fig.4. Comparison among (a) the mean diagonal elements of the a posteriori seismic standard deviation, (b) the mean diagonal elements of the assigned Cmm covariance matrix (takes in account the error propagation from the velocity model to the density model and (c) the mean density update of the first iteration ($\Delta\rho$).

Figure 5

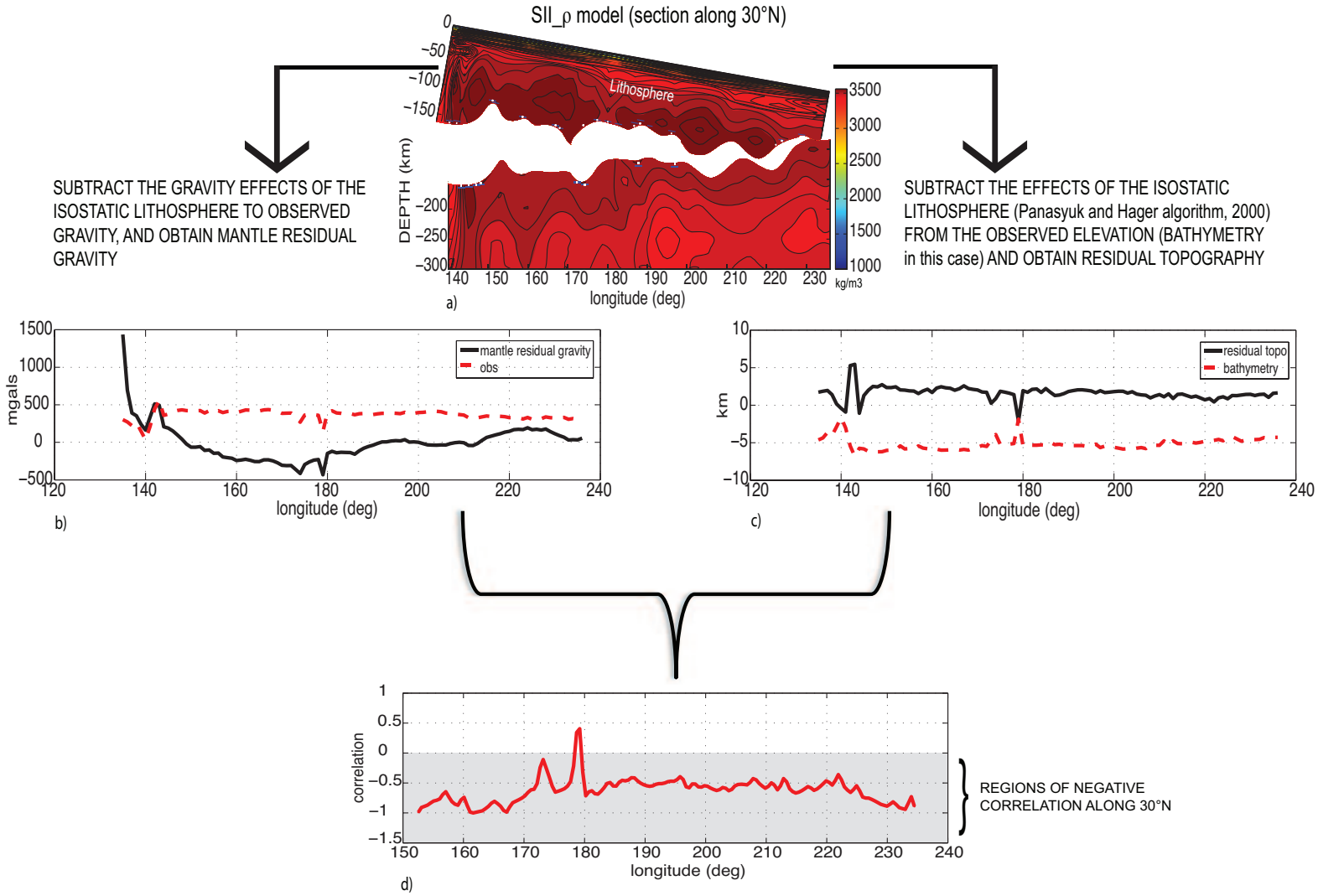

Fig. 5: Sketch of the followed steps to recover (d) the diagonal values of the correlation matrix between the residual topography and the mantle residual gravity anomalies produced by the SII-ρ model. As an example, (a) a vertical slice through the recovered model (30° N) is analysed. The method used to determine the depth of the lithosphere is explained in the text. Following Pekeris (1935) and Hager et al., (1985), the negative correlation between (b) the mantle residual gravity anomaly and (c) the residual topography, may identify the regions where is active the contribution of mantle circulation in supporting the long-wavelength topography is active.

Figure 6

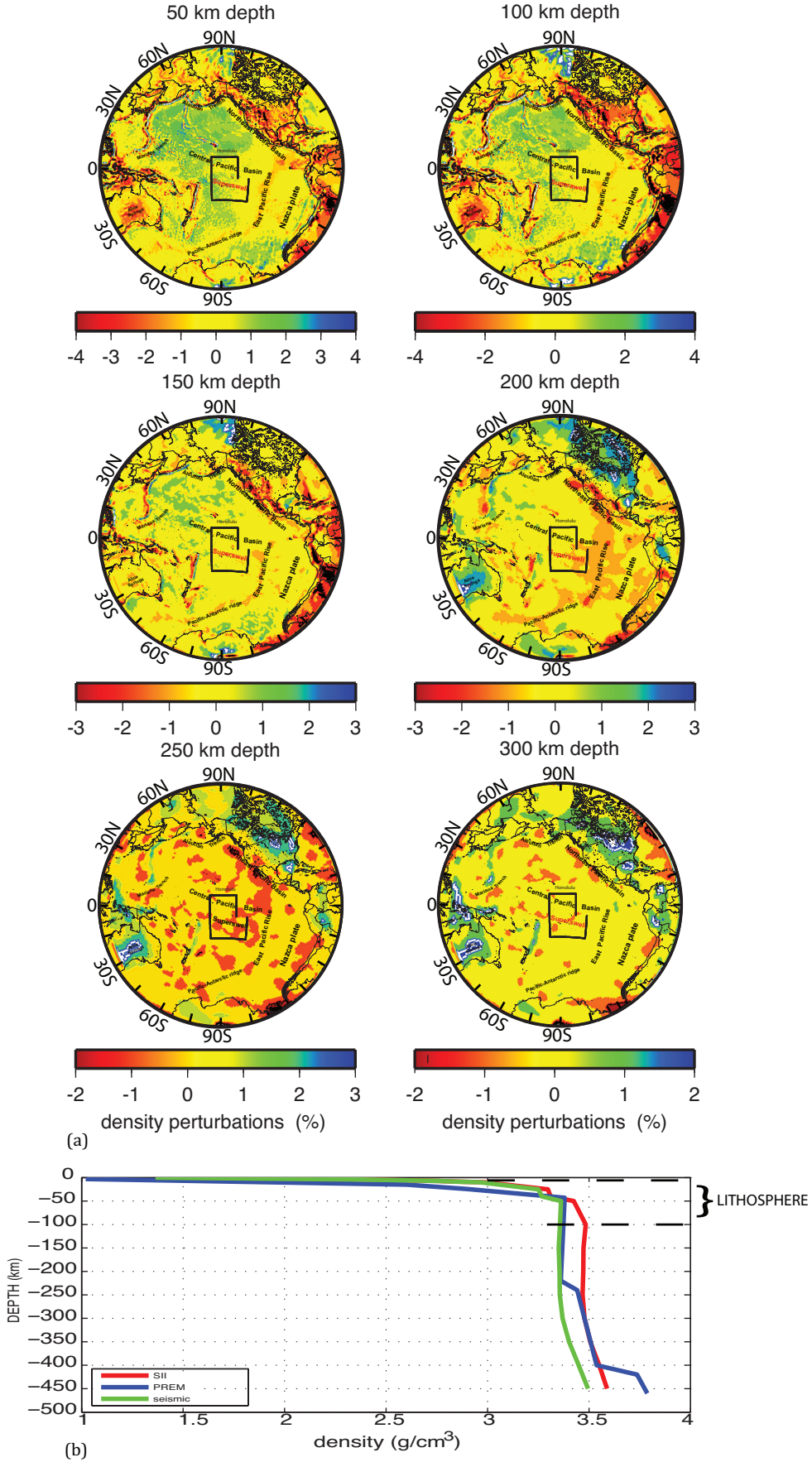

Fig. 6. Depth sections of the ρ percentage perturbations in (a) our optimized SII-ρ model. Model perturbations are expressed as percentage deviations with respect to (b) the mean density value of each layer. In each section, the main tectonic units are indicated. In (b) is indicated the depth interval of the lithosphere in 1D SII-ρ, PREM and seismic model (Maggi et al., 2006) are shown. The area of the Pacific Superswell, identified by Adam and Bonneville (2005) is superimposed.

Figure 7

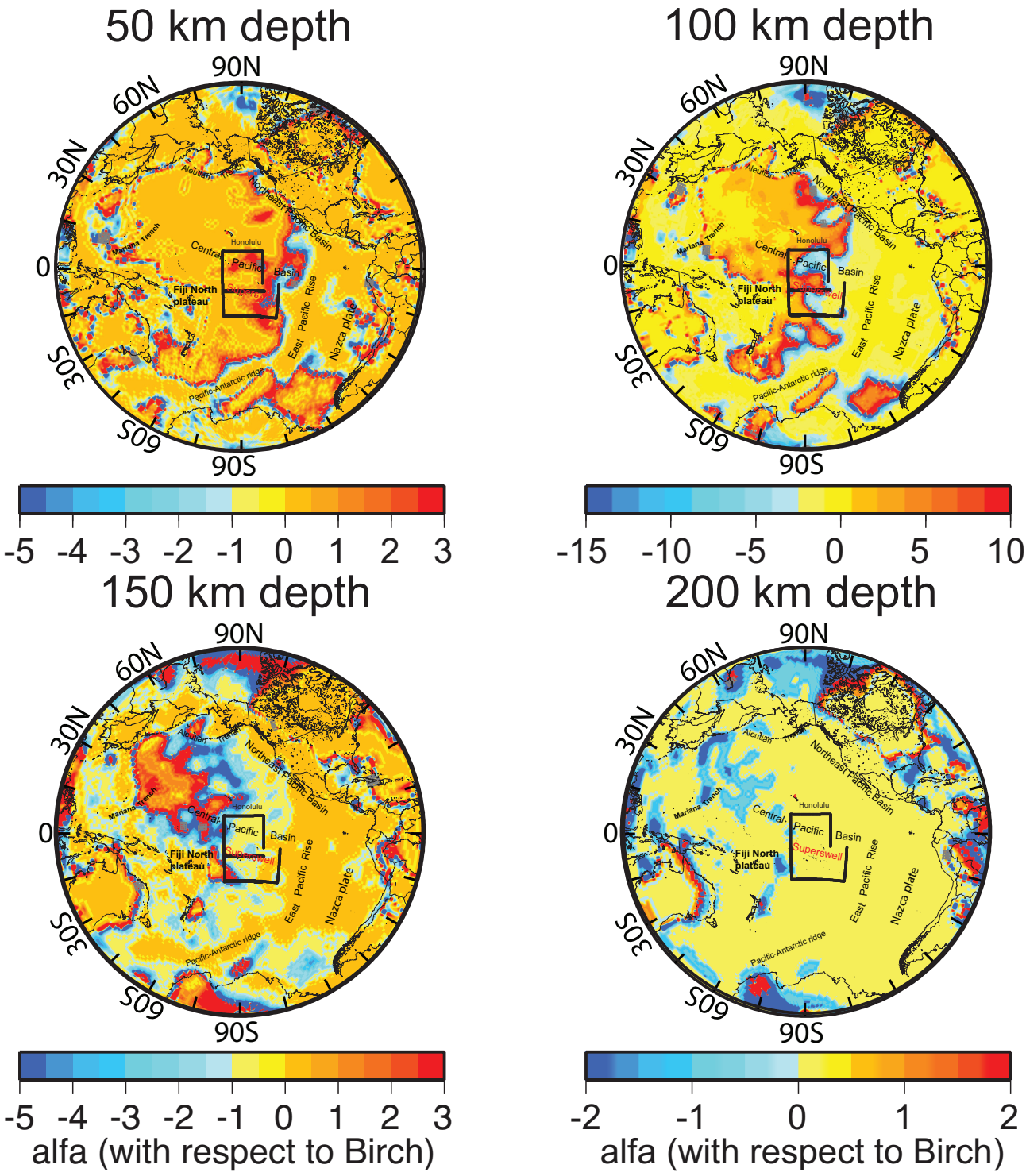

Fig. 7. Depth sections of the lateral differences in the optimized angular coefficient a with respect to the a priori Birch coefficients (0.72 for 50 km depth, 0.34 from 100 to 200 km depth). The area of the Pacific Superswell, identified by Adam and Bonneville (2005) is superimposed on each section.

Figure 8

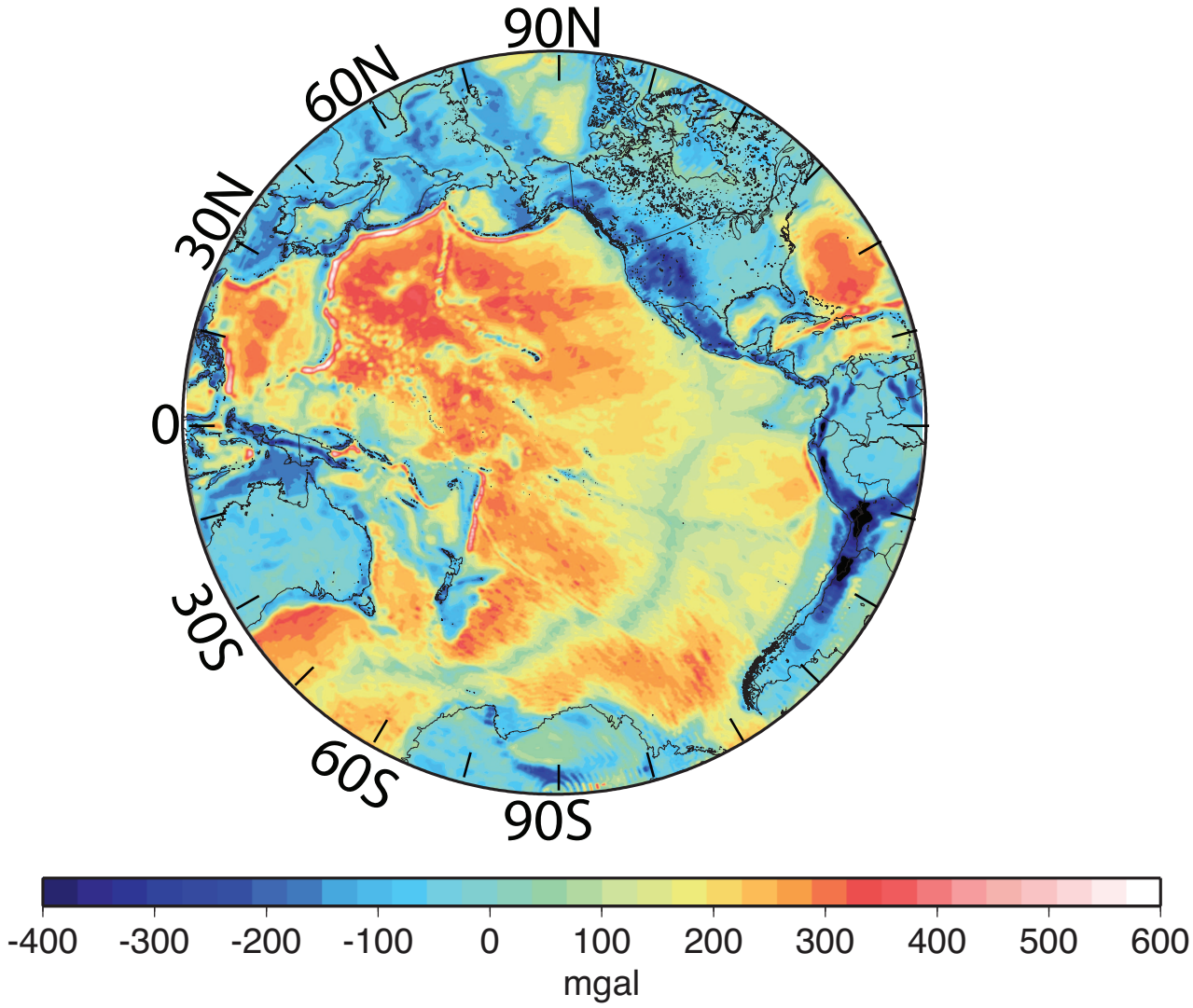

Figure 8. Bouguer anomaly map reproduced by SII-ρ model in Fig. 6 (a). Gravity misfit with respect to observations in Fig. 2 (b) is 66.73 mgals and variance reduction is 67.4%.

Figure 9

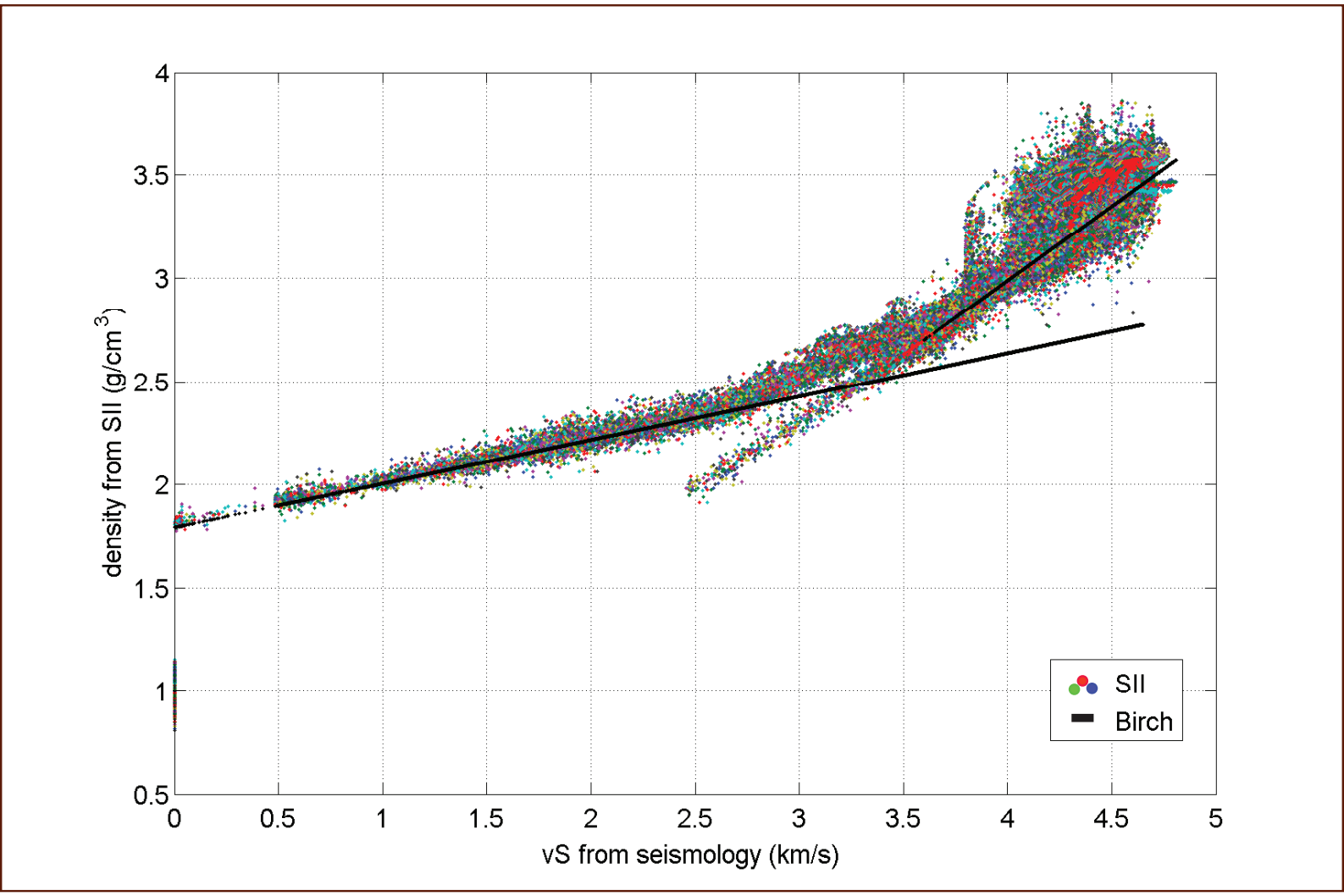

Fig.9. Density values from the recovered SII-ρ model in Fig. 6(a), plotted against the velocity values from the seismological model and compared to Birch law regression lines (black solid lines), our v_SVm^0 - ρ_m^0 starting relationship.

Figure 10

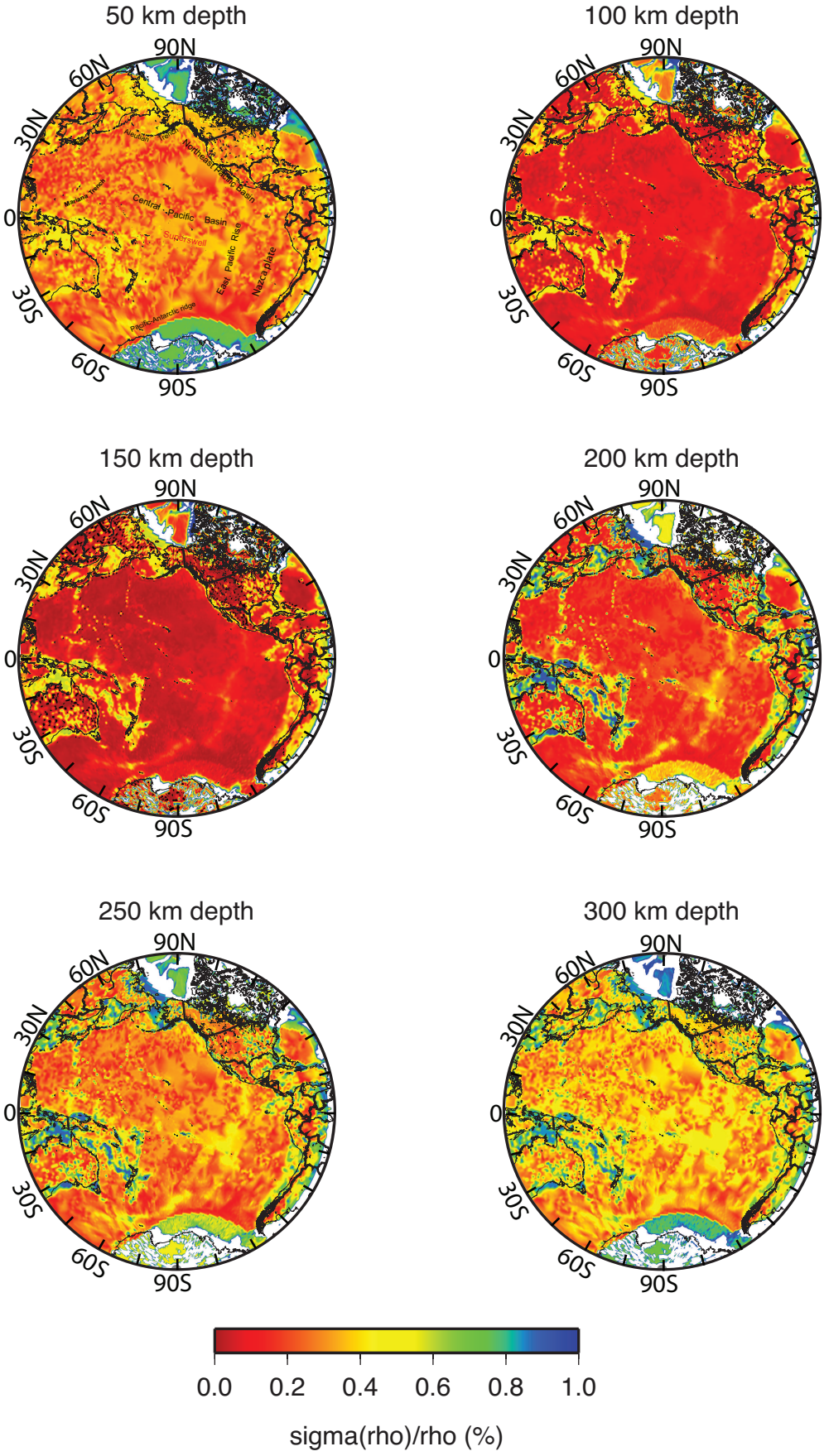

Fig. 10. Depth sections of *a-posteriori* percentage standard deviation on SII-ρ model. Standard deviation takes into account the propagation of uncertainty from the velocity to the density model, weighted with the final gravity variance reduction Var(g(n)), and the information given by the gravity data (eq. (8)). In each section, the standard deviation values are referred to the 1D SII-ρ model imaged in Fig. 6 (b). In the first section, the main tectonic units are indicated.

Figure 11

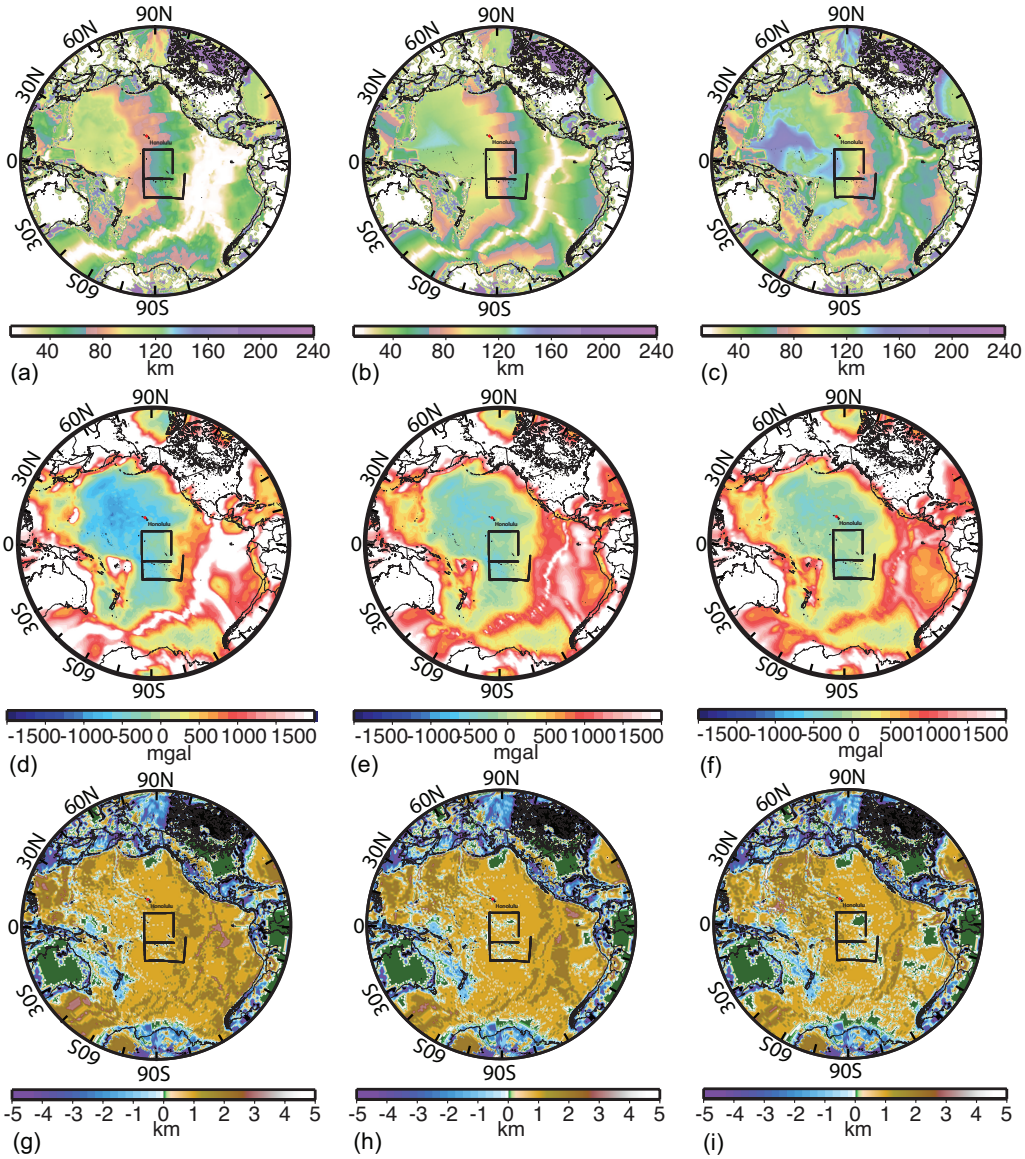

Fig. 11. (a), (b) (c) Calculated lithospheric thickness of the Pacific region, derived mostly from Müller et al., (2008) isochrones (see text for additional information). (b) shows the mean value and (a) and (c) show the mean value minus and plus the standard deviation respectively. (d), (e), (f) Mantle residual gravity anomalies (background density is adjusted in order to magnify the contrast between ocean and continents) calculated assuming the SII density model and the lithospheric depth in (a), (b) and (c). (g),(h),(i) Residual topography of the Pacific region, calculated assuming the SII-ρ density model and the lithospheric depth in (a), (b) and (c).The area of the Pacific Superswell, identified by Adam and Bonneville (2005) is superimposed on each section.

Figure 12

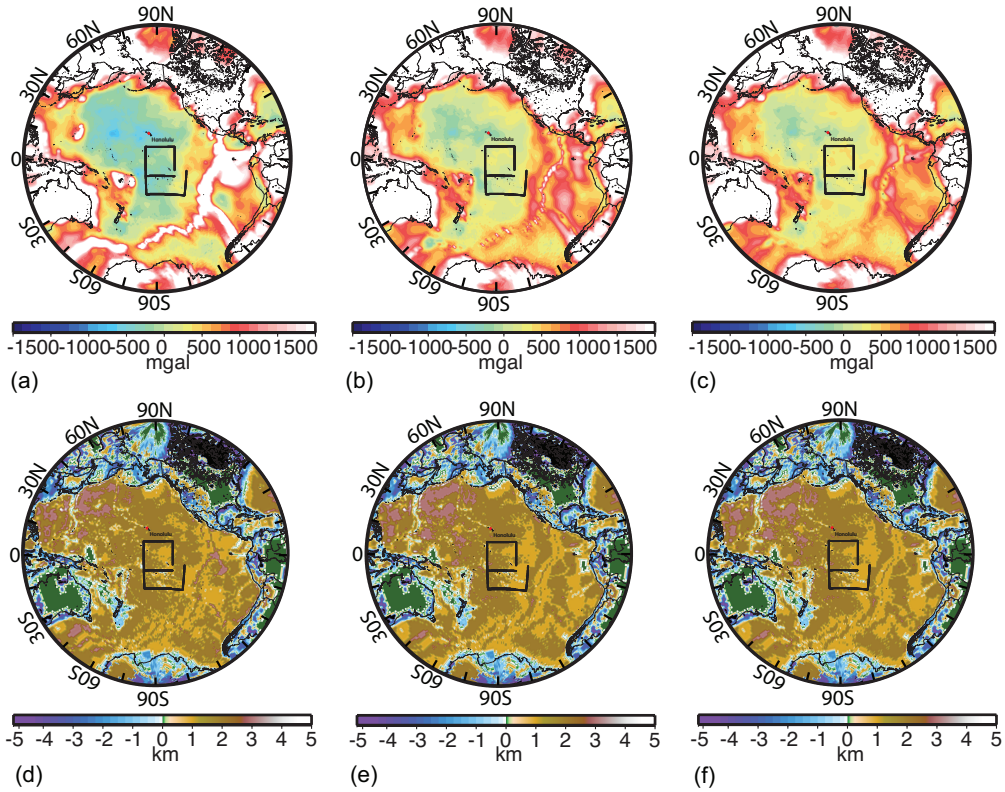

Fig. 12. (a), (b) (c) Mantle residual gravity anomalies calculated assuming that the seismic model has been transformed into a density model through the starting ρ-vSV depth-dependent relationships and the lithospheric depths in Fig. 11 (a), (b) and (c); (d), (e), (f) Residual topography of the Pacific region, calculated assuming that the seismic model has been transformed into a density model through the starting ρ-vSV depth-dependent relationships and the lithospheric depths in Fig. 11 (a), (b) and (c). The area of the Pacific Superswell, identified by Adam and Bonneville (2005) is superimposed on each section.

Figure 13

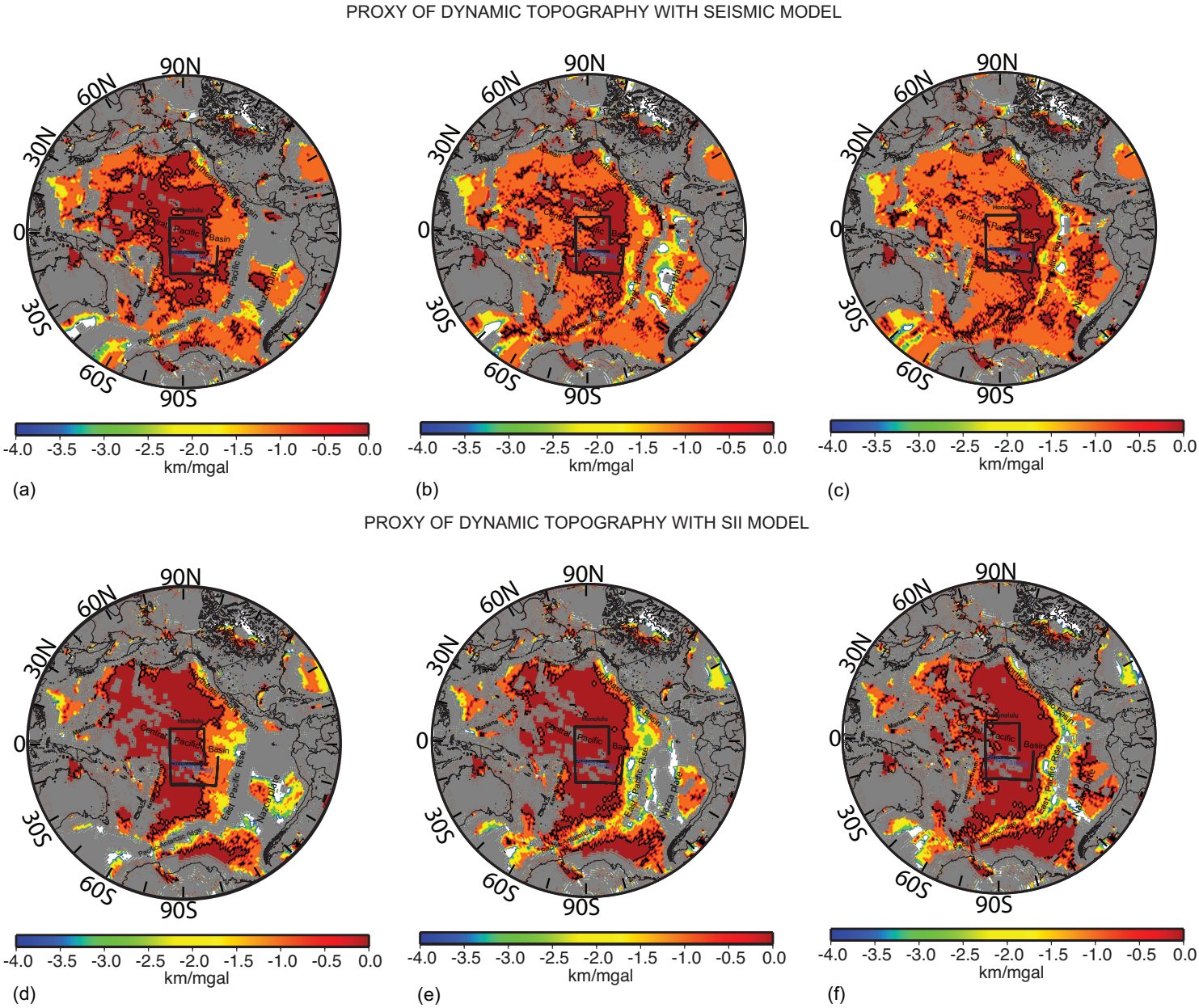

Fig. 13: (a), (b), (c) Proxy of dynamic topography for the seismic model transformed in a density model through the starting ρ-vSVdepth-dependent relationship. Lithospheric depth is referred to Fig. 11 (a), (b) and (c).
(d), (e), (f) Proxy of dynamic topography for the SII density model. Contour plots highlight the areas of negative relationship betweenthe residual topography (subtracted by mean + standard deviation) and the mantle residual gravity (subtracted by mean + standard deviation) of the Pacific region. The area of the Pacific Superswell, identified by Adam and Bonneville (2005) is superimposed on each section.

Figure 14

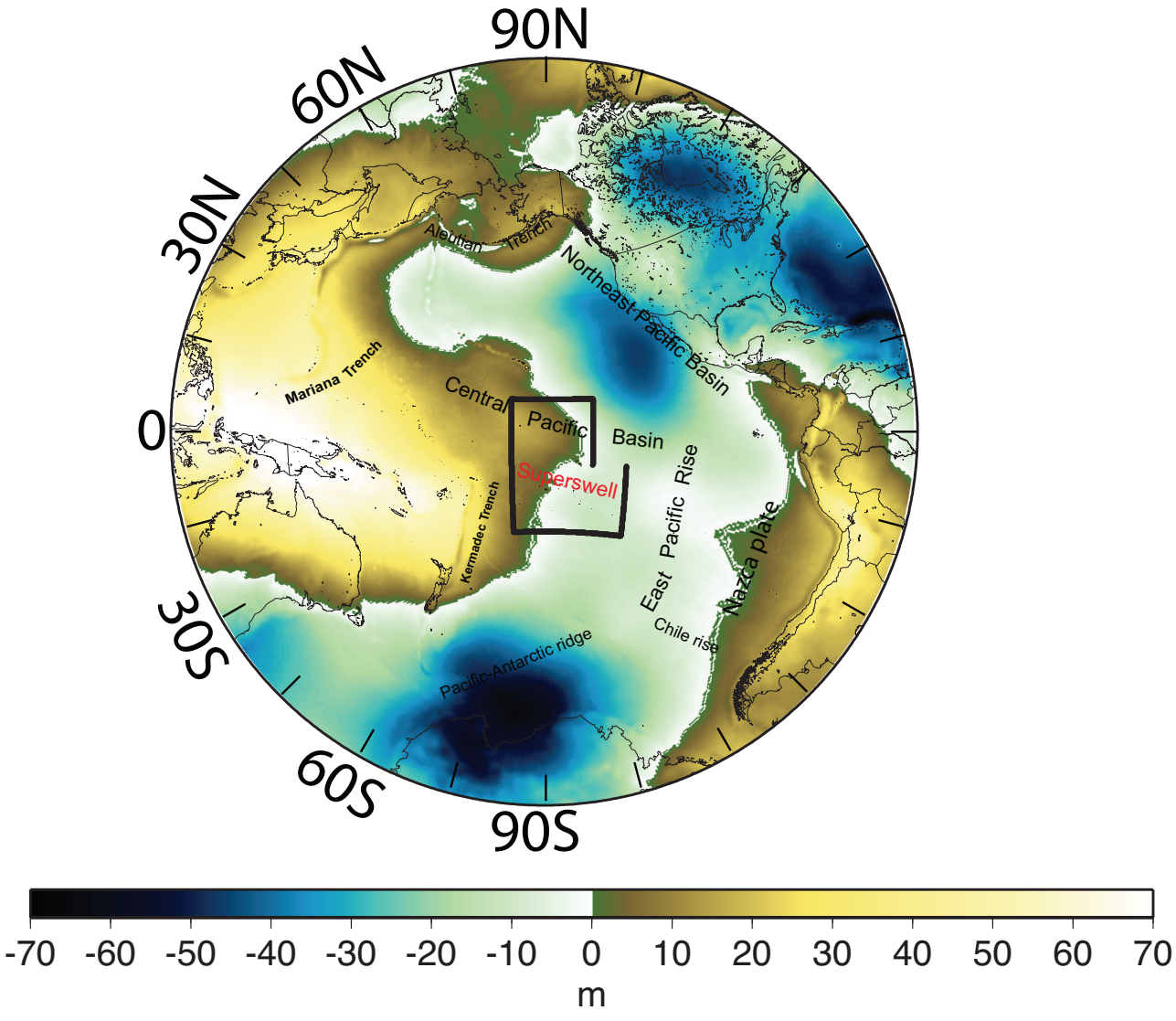

Fig. 14. Geoid ondulations from the combined GOCE-EGM2008 model over the study area. Minimum value is -68,4728 m, maximum value is 87,3623 m.The area of the Pacific Superswell, identified by Adam and Bonneville (2005) is superimposed. The main tectonic units are indicated.

Figure 15

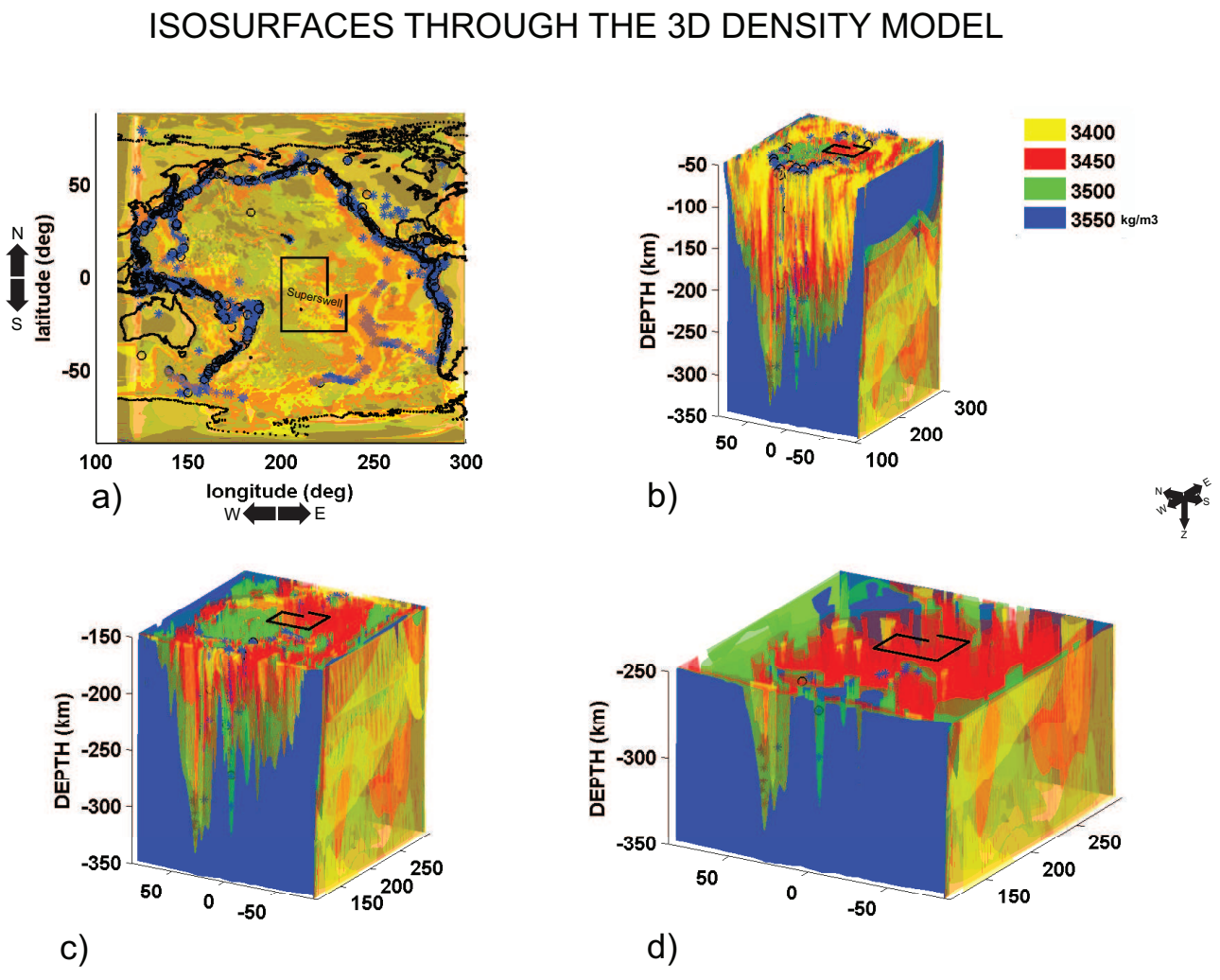

Fig. 15. Isosurfaces of densities characterizing the structures of the upper mantle below the Pacific region as seen (a) directly overhead and in a 3D view (b) cut from 50 km depth, (c) cut from 150 km depth, (d) cut from 250 km depth. Earthquakes from ISC and NEIC catalogues are shown as blue stars for magnitudes between 7.0 and 7.5 and as black circles for magnitude greater than 7.5. The area of the Pacific Superswell, identified by Adam and Bonneville (2005) is superimposed on each plot.